

Static and Dynamic Torque Generation Analysis of a Cable-Actuated Solar Sail

Keegan R. Bunker* and Ryan J. Caverly†
University of Minnesota, Twin Cities, Minneapolis, MN 55455

I. Introduction

SOLAR sails are large space structures consisting of a lightweight sail that utilizes solar radiation pressure (SRP) to produce usable thrust for a spacecraft without requiring fuel of any kind. Though small, this thrust can be used over long durations to enable unique spacecraft mission designs, including interstellar missions [1] and orbits out of the ecliptic plane [2, 3]. If chemical fuel is not used for any other systems onboard the spacecraft, a solar sail can increase the spacecraft operational life span immensely. LightSail 2 showed the potential of solar sails [4], raising its orbital altitude in low Earth orbit from the thrust generated by the sail over the course of its mission. The space community continues to see value in developing solar sails further, as seen by the launch of the Advanced Composite Solar Sail System (ACS3) technology exploration mission into low Earth orbit in 2024 to test novel solar sail boom technologies [5].

Attitude control of solar sails is key to meeting mission requirements, motivating most previous and proposed missions to use reaction wheels as actuators. A typical solar sail attitude control system with reaction wheels includes spinning metal wheels onboard the spacecraft that can generate torques along any direction through the conservation of angular momentum by altering their spin rate. The spin rate has a limited operating range, so another actuator is required to apply a net torque to the spacecraft and allow the reaction wheel speeds to be adjusted without affecting the attitude. This capability is called momentum management. The momentum management requirements will become more challenging as solar sails of substantially larger size are considered for future missions [2, 6], thus requiring larger reaction wheels. Moreover, larger solar sails will likely have more structural flexibility [7–9], resulting in unwanted structural deformations and significant disturbance torques due to imbalances in SRP [10].

Spacecraft missions outside of low Earth orbit typically rely on attitude control system (ASC) thrusters for momentum management, which has also been proposed for solar sails [11, 12]. ACS thrusters use chemical propulsion to apply thrust and generate net torques on the spacecraft. ACS thrusters are in direct opposition to the fuel-free benefits of a solar sail and artificially limit the operational life of a solar sail spacecraft. Several alternative technologies have been investigated to address solar sail momentum management demands without chemical fuel. An effective means to generate momentum management torques that has been extensively explored in the literature involves shifting the

*Ph.D. Student, Department of Aerospace Engineering & Mechanics, 110 Union St. SE, Minneapolis, MN 55455, email: bunke029@umn.edu

†Assistant Professor, Department of Aerospace Engineering & Mechanics, 110 Union St. SE, Minneapolis, MN 55455, AIAA Member, email: rcaverly@umn.edu (Corresponding Author)

solar sail's center of mass using an onboard translation mechanism [12–18]. NASA's Solar Cruiser is equipped with a version of this known as an active mass translator (AMT), which allows for the relative displacement of the upper and lower halves of the solar sail bus [11]. The AMT is capable of generating torques by displacing the center of mass relative to the center of SRP in two axes for momentum management, although it is unclear how this technology will scale up to solar sails with much larger areas due to limits in its range of actuation. Gimballed ballast masses have also been proposed as a means to shift the solar sail's center of mass using a similar concept [19, 20], however, they have remained largely theoretical and may increase the overall mass of the solar sail if the added mass is truly ballast. A variety of concepts involving adjusting the reflectivity properties of portions of the solar sail in order to generate a torque through an imbalance in SRP [21–25] have been proposed. This concept is being considered for use on Solar Cruiser in the form of reflectivity control devices (RCDs) angled from the normal of the solar sail membrane to generate torques out of the plane of the sail [11]. Although this is a promising technology, it produces relatively small torques and comes with the challenge of providing power to devices far from the solar sail bus. Control vanes at the tips of the solar sail's structural booms have been proposed as a means to generate torques similar to the control surfaces on an aircraft [26–30]. Unfortunately, a significant challenge in the use of control vanes is actuating them (most likely with some sort of motor) at the end of long, flexible booms. The control vanes also need to have significant area in order to generate significant torques. In an effort to generate large torques with minimal actuation, it has been proposed to angle the panels of a solar sail [31, 32]. Although this can create large changes in torques, it is only effective when fairly rigid solar sail panels/membranes are used and does not scale well to large lightweight sails. A more practical adaptation of this for large solar sails is the idea of actively shifting the attachment point of the sail membrane quadrant at the end of the boom tip [33]. This can provide large changes in torque, although this also features the challenge of actuation far from the spacecraft bus and can significantly reduce the SRP thrust during actuation. A more detailed description of many of these actuators and other concepts can be found in [1, 34].

The Cable-Actuated Bio-inspired Elastic Solar Sail (CABLESSail) concept, shown in Fig. 1, utilizes controlled deformation of the solar sail's flexible boom structure to change the shape of the sail membrane and produce usable control torques from a differential in SRP. In a sense, CABLESSail aims to transform the undesirable flexible deformations of large solar sails into controlled desirable deformations to generate control torques. Several cables run from the spacecraft bus along each boom, through spreader plates affixed to the booms at set increments, and are fastened to a plate at the end of each boom. Winches within the spacecraft bus pull on these cables to apply tension, which deforms the booms. With coordinated bending, an SRP differential on the sail can generate usable control torques, which is demonstrated in Fig. 2. The control torques generated inherently scale with the size of the solar sail, since the deflection of the sail is used to create these torques, without the need for chemical fuel. Further details on the preliminary concept behind the CABLESSail technology can be found in [35]. This technology shares similarities with the concept in [36, 37] that involves the use of piezoelectric actuation to purposefully deform the solar sail's booms. A major distinction between

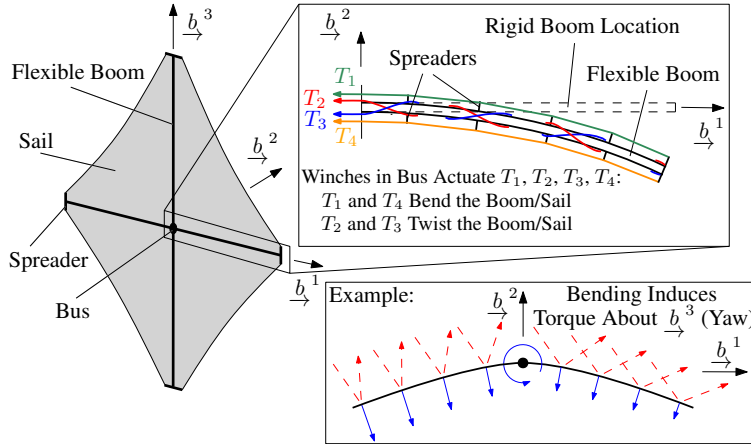


Fig. 1 An overview of the CABLESSail concept. Tensioning cables running through the booms deform the booms and sail shape, generating a net torque from SRP differential.

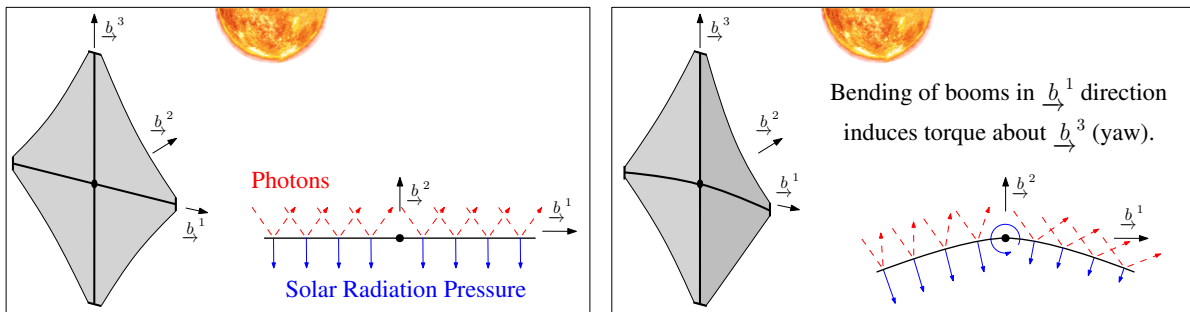


Fig. 2 Torque generation about the pitch/yaw axes of CABLESSail by bending of the booms. The photon incidence angle on each half of the sail is changed and an imbalance in SRP generates the yaw torque.

the CABLESSail concept and the concept in [36, 37] is that cable actuation has the ability to generate much more substantial boom deformations. Additionally, CABLESSail’s actuating cables can hold the boom in a deformed shape without the use of power through a motor brake, unlike the constant voltage needed with piezoelectric actuation.

Three key performance areas are investigated in this note to determine the preliminary capabilities of CABLESSail. Firstly, control of flexible space structures is a challenging area of research [38] and cable-actuated control is even more of a nascent field, so a preliminary analysis of controlled boom tip deflection via basic open-loop cable tensioning is undertaken to assess the potential performance of future feedback boom tip control. The capability of CABLESSail to generate body torques must be comparable to existing technologies to be a worthwhile alternative; therefore, for the second analysis, CABLESSail is directly compared to an AMT. Uncertainty in the shape of the sail membrane has been shown to significantly impact the SRP disturbance torques acting on solar sails in the presence of undesirable boom deflections and is a driver for attitude and momentum control requirements [10]. CABLESSail purposefully makes use of boom deflections to generate SRP torques, so the ability to predictably alter the SRP torque under a wide range of sail membrane shape conditions with coordinated boom bending is examined under the final analysis. The first two analyses

consist of dynamic simulations of CABLESSail and the AMT example solar sail, while the third is a static analyses of CABLESSail assuming steady state control of the boom tips has been achieved.

The novel contribution of this work is a preliminary demonstration of CABLESSail’s capabilities through controlled boom tip deflection. Specifically, these include CABLESSail’s ability to 1) generate a larger attitude change in comparison to an AMT, 2) the ability to reliably generate large pitch and yaw torques under solar sail membrane shape uncertainty, and 3) the ability to reliably generate a large roll torque with some residual pitch and yaw torques under solar sail membrane shape uncertainty. The remainder of this note proceeds with a description of important notation, the definition of Sun incidence angle (SIA) and clock angle, and a summary of the dynamic modeling approach. Four numerical simulation test cases with accompanying results are given in Section IV. Concluding remarks follow in Section V.

II. Preliminaries

This section provides information regarding notation used throughout the note, definitions of the SIA and the clock angle, an overview of the dynamic modeling approach of the solar sail structure, and the SRP solar sail membrane modeling.

A. Notation

The following notation is used throughout this note. A right-handed reference frame of three orthonormal basis vectors, $\underline{a}_1, \underline{a}_2, \underline{a}_3$, makes up reference frame \mathcal{F}_a . The attitude of a reference frame, \mathcal{F}_b , relative to another frame, \mathcal{F}_a , is described through a direction cosine matrix (DCM) $\mathbf{C}_{ba} \in \mathbb{R}^{3 \times 3}$. The DCM is further transcribed into a 3-2-1 Euler angle rotation sequence of principle rotations $\mathbf{C}_{ba} = \mathbf{C}_1(\phi)\mathbf{C}_2(\theta)\mathbf{C}_3(\psi)$ where ϕ , θ , and ψ are yaw, pitch, and roll respectively, with the roll direction chosen such that it aligns with the convention used on NASA solar sail missions. Further details regarding the notation used for physical vectors, reference frames, and DCMs are found in [39, 40].

B. Sun Incidence Angle (SIA) & Clock Angle

The position of the sun relative to the solar sail membrane is a primary driver of SRP force and SRP torque [10]. For the work presented here, the direction of the sun pointing vector that points from the solar sail spacecraft center of mass to the sun is defined by the SIA and the clock angle. SIA is the angle between the sun pointing vector and the vector normal to the solar sail. Clock angle is the angle from a chosen solar sail body fixed vector, which lies in the solar sail plane, to the sun pointing vector projected into this plane. SIA is always a positive value and the sign of the clock angle follows the right handed-convention about the solar sail normal vector.

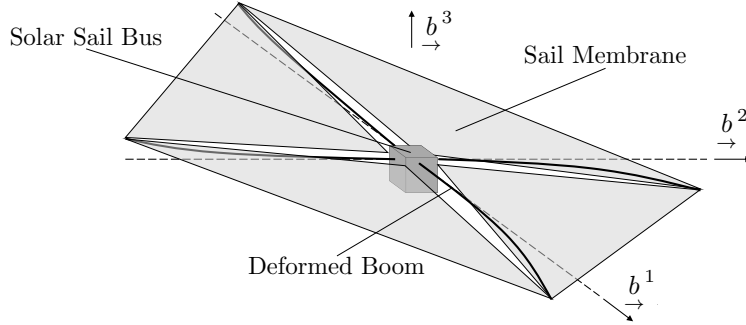


Fig. 3 CABLESSail configuration of assembly # 1 with flat sail membranes constrained to the solar sail bus and deformed boom tips. Undeformed boom positions are shown with dashed lines.

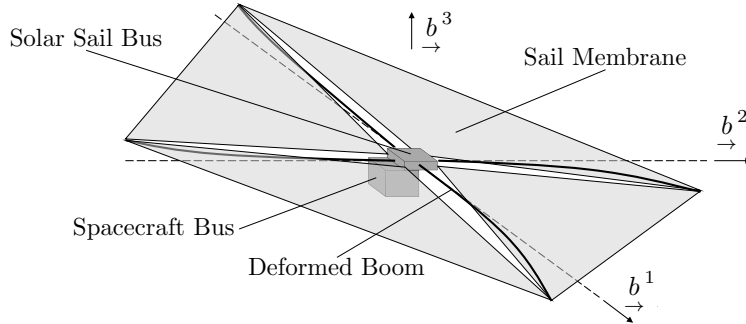


Fig. 4 Solar sail Assembly #2 with the additional spacecraft bus component to represent an AMT with flat sail membranes constrained to the solar sail bus and deformed boom tips.

III. Solar Sail Modeling

Modeling of the solar sail is divided into two parts. The dynamic modeling is summarized with a description of the two solar sail models considered in this work, and the SRP and solar sail membrane shape modeling approach are shown.

A. Solar Sail Assemblies

Two solar sail models are assembled with this modeling approach for comparison in the work presented here, referred to as Assembly #1 and Assembly #2. The former is the default CABLESSail design consisting of four boom components and the solar sail bus component. Assembly #2 ignores the cable actuation within the booms but incorporates an AMT by including the spacecraft bus component and modifying the solar sail bus component. A static offset between these two busses is applied during the assembly step of the dynamic modeling and represents the actuation of the AMT. A depiction of both solar sail models is shown in Fig. 3 and Fig. 4. Specific material and design values are provided in Section IV.

B. Dynamic Modeling Overview

The dynamic modeling approach used in this work is covered in detail in [41] and summarized here for brevity. Dynamic modeling of the solar sail is accomplished by first modeling the dynamics of each solar sail component

individually. These components are the solar sail bus that would house the sail membrane and booms prior to deployment, the four CABLESSail booms that are the primary application of the CABLESSail technology, and the optional spacecraft bus that allows the solar sail bus to be split into two halves for the use of an AMT. The solar sail membrane is not modeled dynamically as a component, rather the SRP force and torque are computed via a solar sail membrane shape model defined in Section III.C and applied to the solar sail bus component. The booms are modeled with Euler-Bernoulli beam theory and the assumed modes method, with the cables imparting vertical loads at the location of the spreader plates as tension is applied. The two busses are modeled as uniform rigid bodies. All chosen components are then constrained together to form the entire solar sail according to the chosen solar sail spacecraft design. The resulting model is highly adaptable to modeling changes and enables a numerical simulation of the position, attitude, and boom deflections for given initial conditions and time-varying cable tension inputs.

C. Solar Sail Membrane Modeling

The solar sail membrane is modeled as four triangular quadrants, each attached at the two respective boom tips and the solar sail bus center of mass. Nominally the sail is flat with zero deflection out of the plane defined by the three aforementioned boundary constraint points. The continuous surface is represented as a triangular point mesh of a chosen density. The static sail deflection of each mesh point out of this plane is defined by the basis function

$$z_{sail}(r, \theta) = \Delta z_{max} \sin\left(\frac{3r\pi\sqrt{2}}{4L}\right) \sin\left(\frac{\theta - \theta_j}{\theta_{j+1} - \theta_j}\right), \quad (1)$$

where $r = \sqrt{x^2 + y^2}$, $\theta = \arctan(y/x)$, Δz_{max} is the chosen maximum out of plane sail membrane deflection, and $\theta_j = (j - 1)\frac{\pi}{2}$ for $j \in [1, 5]$, where j corresponds to the boom number as depicted in Fig. 5. The first boom is double counted within this formulation to account for the wrapping of the angle $\theta = 0$ rad and $\theta = 2\pi$ rad representing the same boom. This basis function is a modification from [10]. The point of highest deflection due to (1) occurs at the centroid of the planar sail quadrant similar to observed sail billowing behavior [10]. The moments of inertia of the sail membrane about the center of mass of the solar sail bus are added to said bus, along with the total sail mass to approximate the inertia properties.

The force exerted on each triangular sail mesh element by the local SRP is applied at the element's planar centroid and modeled as a normal force, F_n , and tangential force, F_t , given by [42]

$$F_t = -PA(1 - rs) \cos(\alpha) \sin(\alpha),$$

$$F_n = -PA(1 - rs) \cos^2(\alpha) - PAB_f(1 - s)r \cos(\alpha) - PA(1 - r) \cos(\alpha) \left(\frac{e_f B_f - e_b B_b}{e_f + e_b} \right),$$

where P is the solar pressure at one astronomical unit (au), A is the sail element area, r is the reflection coefficient, s is

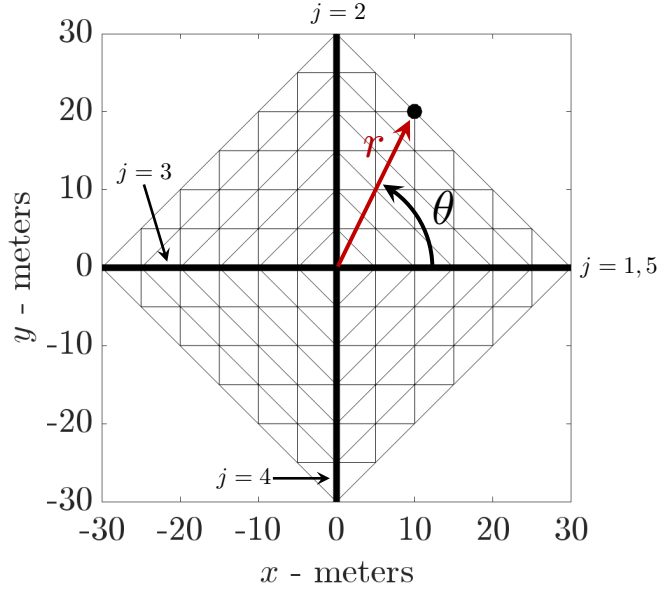


Fig. 5 Top-down view of the triangular solar sail membrane mesh with booms along the x and y directions corresponding to b_1 and b_2 directions accordingly.

the fraction of specular reflection coefficient, α is the local Sun incidence angle (SIA), B_b and B_f are the back and front non-Lambertian coefficients, and e_b and e_f are the back and front surface emissivity, respectively. The sail element area A and local Sun incidence angle α are dependent on the state of the solar sail. All other parameters are constant and listed in Table 1 based on the coefficients in [42]. The forces acting on all elemental centroids are represented in the model by a single force-couple pair applied at the center of mass of the solar sail bus with all respective moment arms due to the respective sail element centroid locations accounted for. This force and couple are referred to as the SRP force and SRP torque, respectively, representing the total thrust generated by the sail membrane and any torques generated due to misalignment of the SRP center of pressure and spacecraft center of mass.

This approach has the affect of decoupling the sail membrane from the structural dynamics and treating SRP as an external generalized force, as internal forces between the booms and the sail are not modeled. Dynamic sail modeling considering these internal forces and dynamic membrane shapes is an open field of research [43, 44]. A simplified model is used here to preserve simulation efficiency and demonstrate the modular structure of the numerical simulation. Said modular structure allows for this external force model to easily be replaced by a more sophisticated technique.

Coefficient	P	r	s	B_b	B_f	e_b	e_f
Value	$4.5391 \times 10^{-6} \text{ N/m}^2$	0.91	0.94	0.67	0.79	0.27	0.025

Table 1 Solar sail optical coefficients derived in [42] that are used in the numerical simulations of Section IV.

IV. Numerical Simulation & Results

Numerical simulations of CABLESSail implementing the modular dynamic modeling approach presented in this note are conducted to investigate the CABLESSail design. First, the impact of non-flat solar sail membrane conditions on SRP torque is tested through a static analysis of deflected booms and varying sail membrane shape. Next, the ability to control boom tip deflection is tested under a dynamic simulation with mock open-loop tension control. The ability of CABLESSail to alter the spacecraft attitude is compared to existing technology in a dynamic simulation. Finally, the capability of CABLESSail to alter the SRP torque through boom deflection is tested under random sail shape conditions through a Monte Carlo test.

Material and design values for the boom components used in Assembly #1 and Assembly #2 are listed in Table 2. All values are identical to those used in [41], except for the flexural rigidity, which is increased for this work to better represent the booms designed for Solar Cruiser [45]. Table 3 contains the dimensions and masses of the busses used for Assembly #1 and Assembly #2. Note that the busses for Assembly #2 account for the same overall mass and dimension as the single bus used for Assembly #1, such that both solar sail assemblies have identical inertial properties when the AMT offset between the busses in Assembly #2 is zero. The prescribed offset is noted in the relevant test cases.

Symbol	Parameter	Value
L	Boom Length	29.5 m
R	Boom Radius	0.1 m
m_{B_i}	Boom Mass	3 kg
ρ	Boom Linear Density	0.1017 kg/m ²
EI	Flexural Rigidity	1700 Nm ²
h	Spreader plate distance beyond boom radius	0.1 m
-	Number of Plates	19
Δx	Plate Spacing	1.5526 m
m_{sail}	Solar Sail Mass	50 kg

Table 2 Material and component constants used throughout the numerical simulations in Section IV.

	Solar Sail Bus	Spacecraft Bus
Assembly #1	$h = 100$ cm, $w = 30$ cm, $d = 30$ cm mass = 100 kg	
Assembly #2	$h = 10$ cm, $w = 30$ cm, $d = 30$ cm mass = 50 kg	$h = 90$ cm, $w = 30$ cm, $d = 30$ cm mass = 50 kg

Table 3 Solar sail bus and spacecraft bus dimensions and mass for Assembly #1 and Assembly #2.

Initial conditions for all test cases are assumed to be the following unless stated otherwise; zero translational velocity, zero rotational velocity, zero boom tip deflection, zero applied cable tension, and zero SIA, with the three-axis, \underline{b}_3 of

the solar sail bus aligned with the local Sun pointing vector. The distance from the Sun for all cases is 1 astronomical unit (au), or the mean radius of Earth’s orbit. Amplitudes for the solar sail membrane quadrants, following the approach described in Section III.C, are specified for each test case. To assist with computational efficiency, artificial structural damping is added to the numerical simulation as described in [41] such that the damping ratio on all modes of the linear system do not exceed 1%.

A. Sail Shape Effect on SRP Torque

The SRP torque produced by Assembly #1 under static boom deflection and two different solar sail membrane shapes is computed across all clock angles and an SIA of 30° . First, a flat solar sail membrane with $\Delta z_{max} = 0$ for each quadrant is considered, and the second has a non-flat membrane with the membrane function amplitudes for each quadrant, Δz , drawn independently from a uniform distribution on the open range $(-30.0 \text{ cm}, 0.0 \text{ cm})$. These membranes shapes are shown in Fig. 6. The SRP torque produced by both sails across all clock angles is shown in Fig. 7. At a high SIA the flat membrane with symmetric tip deflection produced zero roll torque across all clock angles with a sinusoidal pattern across the pitch and yaw directions, indicating the torque vector was of constant magnitude and lain within the sail plane at all clock angles. Conversely, the non-flat membrane produced non-zero roll torques and distorted the pattern in the pitch and yaw directions. These results agree qualitatively with the SRP torque and sail shape relations outlined in [10], which considered a sail membrane constrained along the entire boom length, rather than the tip and base as shown here.

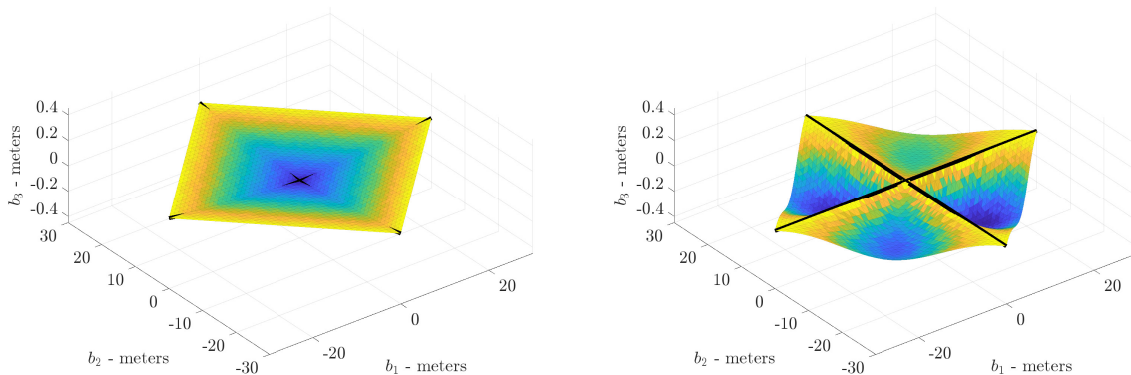


Fig. 6 The two solar sail membrane shapes used to examine the effect of sail shape on SRP torque, including a nominal flat sail and a deformed sail membrane.

B. CABLESSail Tension Input

A numerical simulation of Assembly #1 is conducted with a flat membrane for each quadrant ($\Delta z = 0$). All cable tensions are kept zero except for the cable on boom B_c , where a linear ramp in tension is applied across the first minute

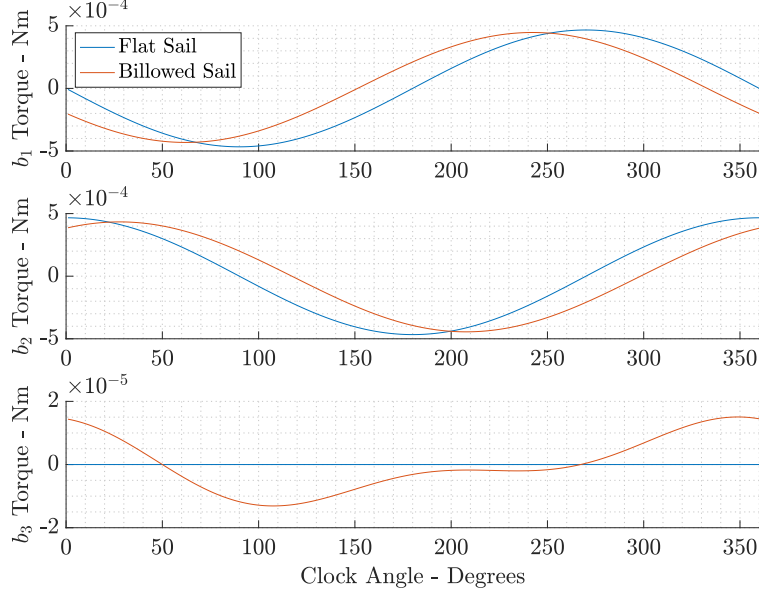


Fig. 7 SRP torque generated by both solar sail membrane shapes across all clock angles at an SIA of 30° and resolved in the body fixed frame, \mathcal{F}_b .

of the simulation, ending at a value of 4.0 N. The final tension is held constant for 29 additional minutes following the linear ramp, where the simulation is then concluded after a total elapsed time of 30 minutes. Time histories of the out-of-plane boom tip deflections and the resulting SRP torque applied to the assembly, resolved in the solar sail bus frame, are shown in Fig. 8.

It can be seen that oscillations are present in all boom tip deflections, indicative of vibrations in the whole structure once a non-zero open-loop cable tension is applied without consideration for the resulting dynamic response. These vibrations are carried forward into the SRP torques due to the boom tip sail attachment points. Vibrations are expected with actuation of flexible structures, but are generally undesirable for momentum management torques, so active feedback control of the structure will be required to eliminate this behavior. Torque of this magnitude is comparable to other momentum management technologies for solar sails of this size [11].

C. AMT vs CABLESSail Attitude Change

Two numerical simulations are conducted of the Assembly #1 and Assembly #2 models individually with nominal initial conditions. Assembly #1 in the first simulation begins with zero cable tensions, then an identical linear ramp in tension to that described in Section IV.B is applied to a single cable, bending boom B_c out of the sail plane towards the Sun-facing direction. Assembly #2 in the second simulation utilizes a constant offset between the spacecraft bus and the solar sail bus, such that the center of mass of B_g is 30 cm offset from the center of mass of B_b in the \underline{b}_1 direction, which is consistent with the maximum achievable offset by Solar Cruiser's AMT [11, 46]. No tension is applied to any cables within the Assembly #2 model for the duration of the simulation. Both models are simulated for 30 minutes,

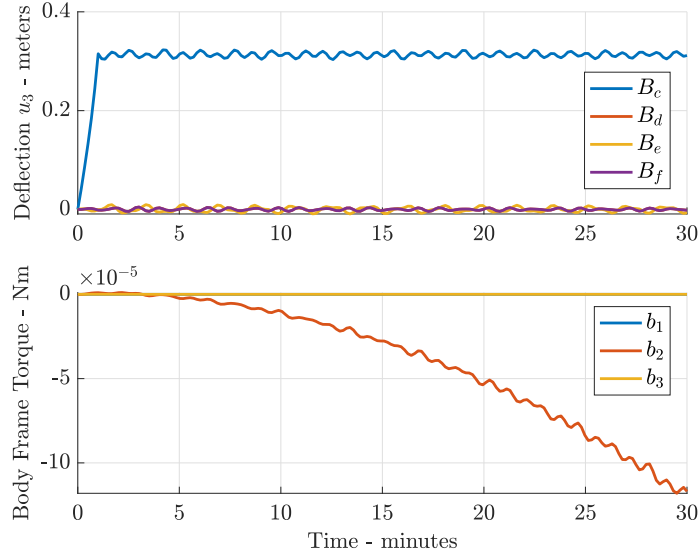


Fig. 8 Time history of the out-of-plane boom tip deflections and resulting SRP body torques resolved in the solar sail bus frame, \mathcal{F}_b , subject to a one minute linear ramp in tension followed by a constant tension in one cable.

and the attitude time history is shown in Fig. 9 as Euler angles. It can be seen that the CABLESSail boom actuation of Assembly #1 meets and then exceeds the yaw angle change of the AMT in Assembly #2. The attitude profile of the Assembly #1 simulation shows an increasing rate of change in the yaw angle, while the Assembly #2 simulation shows a roughly constant yaw rate across this testing window. This provides confidence that even a small tension in CABLESSail’s actuating cable is an effective means to control the solar sail’s attitude in comparison to the use of an AMT.

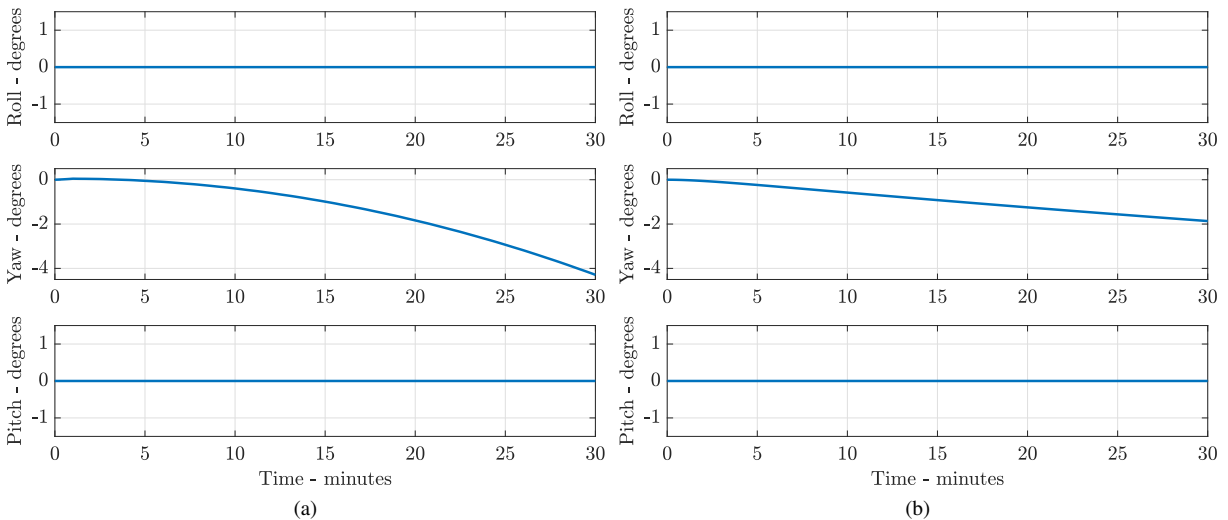


Fig. 9 Euler angle time histories (a) of Assembly #1 generating SRP torque through cable tensioning and deflection of one boom and (b) Assembly #2 with a static AMT actuation of 30 cm spacecraft bus offset.

D. CABLESSail SRP Torque Change Capability

A Monte Carlo test is conducted with the static model of Assembly #1 to demonstrate the capability of CABLESSail to alter the SRP torque produced from coordinated boom deflections under unknown sail membrane shape conditions. Two specific boom deflection combinations are identified for examination: one likely to produce torques in the pitch-yaw directions by deforming two booms and one likely to produce torques in the roll direction by deforming all booms. These two combinations, or maneuvers, begin with a nominal boom tip deflection of 10 cm then apply a 20 cm magnitude cable-actuated tip deflection to the identified booms in either the positive or negative direction. The nominal boom tip deflection is chosen to be representative of the worst-case thermal deformations expected for Solar Cruiser's booms [10]. To represent the membrane shape uncertainty, ten thousand random sail membrane shapes are generated by independently sampling membrane function amplitudes, Δz , for each quadrant from a uniform distribution on the open range (-30.0 cm, 0.0 cm).

To assess the torque change capability under a reasonable set of attitude conditions, a single SIA and clock angle pair of 17° and 0° are considered for both maneuvers. This clock angle is such that the vector pointing towards the Sun from the solar sail center of mass lies within the $\underline{b}_1 - \underline{b}_3$ plane. The nominal SRP torque is calculated for each sail membrane under nominal boom tip deflections. The first boom maneuver is then applied through the respective static tip deflections, the SRP torque is recomputed, and the difference is taken with respect to the nominal SRP torque previously recorded. This process is repeated for both boom maneuvers and every sail membrane.

1. Pitch - Yaw Torque Generation

The first boom-maneuver consists of booms on opposite sides of the solar sail bus deformed in opposite directions, one towards the Sun and one away, while the remaining two booms are left at the nominal deflection. This deformed sail structure is shown in Fig. 10. Change in SRP torque along each solar sail bus body axis for all ten thousand membrane cases at the prescribed SIA and clock angle is shown in Fig. 11 as a binned histogram. For all membrane cases there is a consistent negative change in SRP torque along the \underline{b}_2 direction. This is considered a pitch torque, as it lies in the nominal flat plane of the solar sail. There is a small change in SRP torque along the \underline{b}_3 direction relative to the change seen in the \underline{b}_2 direction. This \underline{b}_3 torque is referred to as a roll torque for the solar sail.

Given the reliable generation of a relatively large pitch torque with minimal yaw torque and roll torque, this particular maneuver shows great promise in situations where a pitch torque is required for attitude control or momentum management. As the boom structure of the solar sail is symmetric and the membrane shapes are random, this result can be extrapolated for any clock angle aligning with a pair of booms (0° , 90° , 180° , 270°) and deforming the appropriate booms according to this maneuver. This result shows promising evidence of CABLESSail capability to counteract SRP disturbance torques, with the average pitch torque change of all test cases exceeding the maximum pitch-yaw disturbance torque expected at this SIA for Solar Cruiser [10].

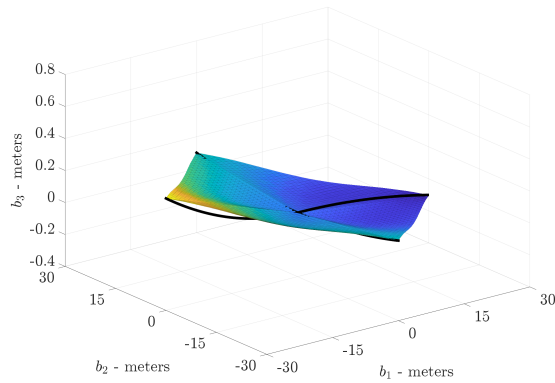


Fig. 10 Static CABLESSail boom deformations under the first boom maneuver, where the booms along the positive and negative \underline{b}^1 direction are deflected by -20 cm and 20 cm, respectively.

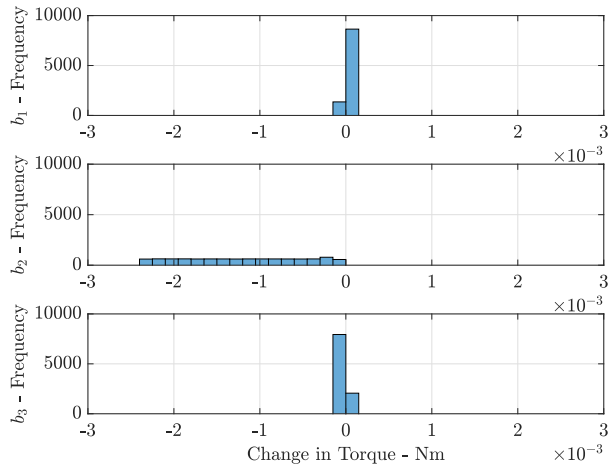


Fig. 11 Histogram reporting the change in SRP torque along the \mathcal{F}_b directions after applying the first boom maneuver to 10,000 random sail membrane shapes at a clock angle of 0° and an SIA of 17° .

2. Roll Torque Generation

The second boom-maneuver deflects all four booms, with those parallel to the \underline{b}_1 direction actuated in the positive direction, and the remaining two parallel to the \underline{b}_2 direction actuated in the negative direction. Fig. 12 shows the resulting deformed sail structure. Change in SRP torque along the \underline{b}_1 , \underline{b}_2 , and \underline{b}_3 directions for all ten thousand sail membranes at the prescribed SIA and clock angle are shown in Fig. 13 as a binned histogram. Both positive and negative torque changes are present in the pitch-yaw directions, \underline{b}_1 and \underline{b}_2 , while a negative change in the roll direction, \underline{b}_3 , is present for all cases. Note that the torque changes presented for this maneuver are an order of magnitude lower than the previous.

Although the torques generated by this maneuver in the pitch and yaw axes appear random, it is noteworthy that a reliably large negative roll torque change is generated. Roll torques are notoriously challenging to generate with the actuators available to solar sails while undesired pitch and yaw torques are much simpler to address [11], which makes

this actuation maneuver potentially useful. It is also worth noting that the maximum change in torque generated in the roll axis is on the order of 10^{-4} Nm, which is roughly an order of magnitude larger than the torque capability of Solar Cruiser’s reflectivity control devices [47] and the largest roll disturbance torque predicted for Solar Cruiser [10].

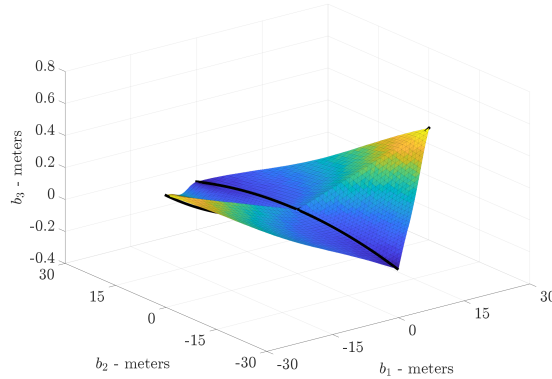


Fig. 12 Static CABLESSail boom deformations under the second boom maneuver, where both booms along \vec{b}^1 are deformed by 20 cm and the two opposite booms along \vec{b}^2 by -20 cm.

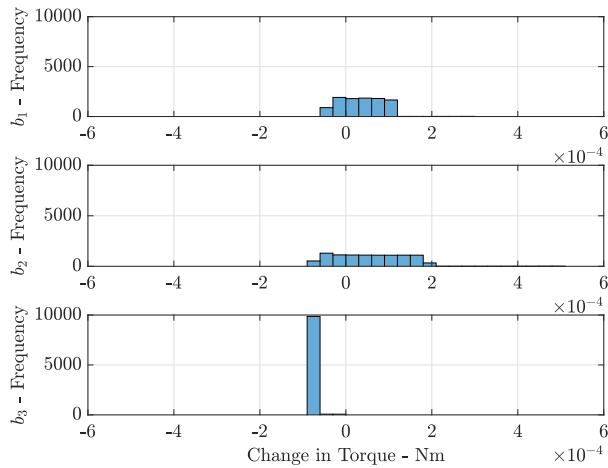


Fig. 13 Histogram reporting the change in SRP torque along the \mathcal{F}_b directions after applying the second boom maneuver to 10,000 random sail membrane shapes at a clock angle of 0° and an SIA of 17° .

V. Conclusions and Future Work

A preliminary analysis of CABLESSail’s capability to generate body torques through controlled boom deflection via actuated cables was presented. The structural dynamics of the solar sail were modeled with a modular multi-body method incorporating cable-actuated flexible booms. A non-flat solar sail membrane was modeled with a variable shape function to compute SRP forces and torques subject to time-varying boom deflection. Through open-loop cable tensioning, CABLESSail surpassed the attitude slewing performance of a fully actuated AMT. Dynamic structural

response to open-loop cable tensioning indicated the need for robust feedback control of boom deflections. CABLESSail demonstrated large roll, pitch, and yaw torque generation at a subset of SIA and clock angles under solar sail membrane shape uncertainty. The pitch and yaw torques generated exceeded the Solar Cruiser disturbance torque requirements, and roll torques were generated with residual pitch and yaw torques.

Future work will focus on the comprehensive analysis of SRP torque change due to CABLESSail's boom deflection across an entire operational range of Sun incidence angles and clock angles under unknown sail membrane conditions. This will allow for the design of a robust control allocation method to determine suitable actuation maneuvers that predictably generate desired SRP torques in all three axes.

Appendix: Component Dynamic Modeling

The individual components are modeled by first identifying the generalized coordinates and velocities, then deriving the component kinetic and potential energies. The generalized forces acting on the components are derived and Lagrange's equation is used to derive the constrained component equations of motion. Finally, the first instance of the null-space method is used to remove the Lagrange multipliers enforcing the attitude parameterization constraint. All components are assumed to be of uniform density, which is not a requirement of the method, but a convenient assumption for the analyses to follow.

VI. Additional Preliminaries: Physical Vectors

The physical vector of the position of point p relative to point w is \underline{r}^{pw} . The velocity of point p relative to point w with the time derivative taken with respect to \mathcal{F}_a is, $\underline{v}^{pw/a} = \underline{r}^{pw/a}$. The angular velocity of \mathcal{F}_b relative to \mathcal{F}_a is $\underline{\omega}^{ba}$. Position, velocity, angular velocity, and all other physical vectors can be resolved in any reference frame. For example, \mathbf{r}_a^{pw} , $\mathbf{v}_a^{pw/a}$, and $\boldsymbol{\omega}_a^{ba}$, represent physical vectors resolved in \mathcal{F}_a .

VII. Attitude Parameterization for Each Component

The attitude of all component bodies, B_i , where $i \in \{b, c, d, e, f, g\}$, is defined as the attitude between the respective component body frame, \mathcal{F}_i , affixed to each body and the inertial frame, \mathcal{F}_a , as expressed through the direction cosine matrix, \mathbf{C}_{ia} . All DCMs are vectorized into a generalized coordinate as column vector \mathbf{p}^{ia} , where $\mathbf{C}_{ia}^\top = \begin{bmatrix} \mathbf{p}_1^{ia} & \mathbf{p}_2^{ia} & \mathbf{p}_3^{ia} \end{bmatrix}$ and $\mathbf{p}^{ia^\top} = \begin{bmatrix} \mathbf{p}_1^{ia^\top} & \mathbf{p}_2^{ia^\top} & \mathbf{p}_3^{ia^\top} \end{bmatrix}$.

The rates of \mathbf{p}^{ia} are related to the angular velocity of \mathcal{F}_i relative to \mathcal{F}_a resolved in \mathcal{F}_i by

$$\dot{\mathbf{p}}^{ia} = \boldsymbol{\Gamma}_i^{ia}(\mathbf{p}^{ia})\boldsymbol{\omega}_i^{ia}, \quad (2)$$

$$\boldsymbol{\omega}_i^{ia} = \mathbf{S}(\mathbf{p}^{ia})\dot{\mathbf{p}}^{ia}, \quad (3)$$

where

$$\mathbf{S}(\mathbf{p}^{ia}) = \mathbf{S}_i^{ia} = \begin{bmatrix} \mathbf{0} & \mathbf{p}_3^{ia^\top} & \mathbf{0} \\ \mathbf{0} & \mathbf{0} & \mathbf{p}_1^{ia^\top} \\ \mathbf{p}_2^{ia^\top} & \mathbf{0} & \mathbf{0} \end{bmatrix}, \quad \boldsymbol{\Gamma}(\mathbf{p}^{ia}) = \boldsymbol{\Gamma}_i^{ia} = \begin{bmatrix} \mathbf{0} & \mathbf{0} & \mathbf{p}_2^{ia} \\ \mathbf{p}_3^{ia} & \mathbf{0} & \mathbf{0} \\ \mathbf{0} & \mathbf{p}_1^{ia} & \mathbf{0} \end{bmatrix},$$

and $\mathbf{S}_i^{ia}\boldsymbol{\Gamma}_i^{ia} = \mathbf{1}$ [48].

VIII. Component Generalized Coordinates & Generalized Velocities

The generalized coordinates of all components include a position vector relative to an inertial point and a vectorized DCM relative to an inertial frame, and the flexible booms utilize elastic coordinates to describe the deformation state. Generalized velocities of all components consist of the respective time derivatives of these coordinates.

A. Solar Sail Bus

The solar sail bus, body B_b , is modeled as a continuous rigid rectangular prism with dimensions h , w , and d , as shown in Fig. 14. Reference frame \mathcal{F}_b is affixed to the body. The \underline{b}_1 , \underline{b}_2 , and \underline{b}_3 directions are referred to throughout the note as yaw, pitch, and roll directions, respectively, for convenience. The plane defined by \underline{b}_1 and \underline{b}_2 is the solar sail plane. The generalized coordinates describing the state of B_b are $\mathbf{q}^{B_b^\top} = \left[\mathbf{r}_a^{ba^\top} \ \mathbf{p}^{ba^\top} \right]$, where \mathbf{r}_a^{ba} is the position of the center of mass of the body relative to an unforced particle a resolved in the inertial frame \mathcal{F}_a , and where \mathbf{p}^{ba} is the vectorized DCM \mathbf{C}_{ba} . The generalized velocities for the unconstrained spacecraft hub component B_b are $\mathbf{v}^{B_b^\top} = \left[\dot{\mathbf{r}}_a^{ba^\top} \ \boldsymbol{\omega}_b^{ba^\top} \right]$, where $\boldsymbol{\omega}_b^{ba}$ is the angular velocity vector of body frame \mathcal{F}_b relative to \mathcal{F}_a resolved in \mathcal{F}_b . These generalized velocities are related to the generalized coordinates through the mappings

$$\dot{\mathbf{q}}^{B_b} = \boldsymbol{\Gamma}_{B_b} \mathbf{v}^{B_b} \quad (4)$$

$$\mathbf{v}^{B_b} = \mathbf{S}_{B_b} \dot{\mathbf{q}}^{B_b} \quad (5)$$

where $\boldsymbol{\Gamma}_{B_b} = \text{diag}\{\mathbf{1}, \boldsymbol{\Gamma}_b^{ba}(\mathbf{p}^{ba})\}$, $\mathbf{S}_{B_b} = \text{diag}\{\mathbf{1}, \mathbf{S}_b^{ba}(\mathbf{p}^{ba})\}$, and $\mathbf{S}_{B_b} \boldsymbol{\Gamma}_{B_b} = \mathbf{1}$. The dimensions and inertial properties of this component are varied in the numerical tests cases and are specified in Section IV.

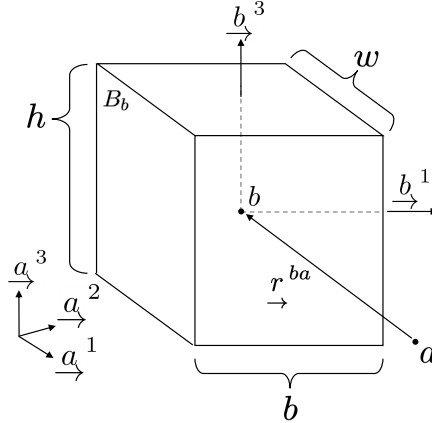


Fig. 14 Solar sail bus component, B_b , with body-fixed reference frame, \mathcal{F}_b , center of mass, b , position relative to the inertial point a , \underline{r}^{ba} , and base, b , height, h , and width, w , dimensions labeled.

B. Spacecraft Bus

The spacecraft bus, body B_g , is modeled as a solid rectangular prism with dimensions h , w , and d , with body fixed reference frame \mathcal{F}_g as show in Fig. 15. The offset between the solar sail bus and spacecraft bus achieved by the AMT is held constant for all test cases in the work presented here, thus the AMT generalized coordinates and the relation to the generalized velocities follow similarly to the spacecraft bus as $\mathbf{q}^{B_g^\top} = [\mathbf{r}_a^{g a^\top} \ \mathbf{p}^{g a^\top}]$, $\mathbf{v}^{B_g^\top} = [\dot{\mathbf{r}}_a^{g a^\top} \ \boldsymbol{\omega}_b^{g a^\top}]$, $\dot{\mathbf{q}}^{B_g} = \boldsymbol{\Gamma}_{B_g} \mathbf{v}^{B_g}$, and $\mathbf{v}^{B_g} = \mathbf{S}_{B_g} \dot{\mathbf{q}}^{B_g}$. The inertial quantities and dimensions are noted in Section IV.

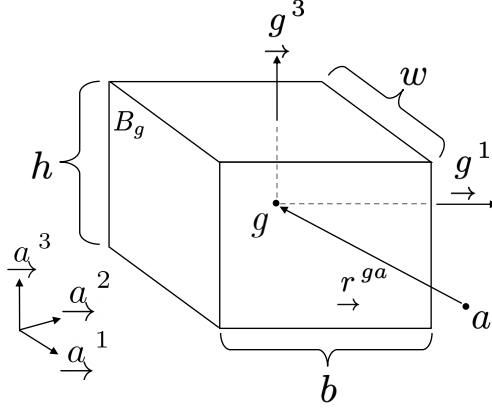


Fig. 15 Spacecraft bus component, B_g , with body-fixed reference frame, \mathcal{F}_g , center of mass, g , position relative to the inertial point a , \underline{r}^{ga} , and base, b , height, h , and width, w , dimensions labeled.

C. CABLESSail Booms

Each flexible boom is modeled as a cantilevered flexible cylinder referred to as body B_i , where $i \in \{c, d, e, f\}$. Reference frame \mathcal{F}_i is affixed to the base of each boom, as shown in Fig. 16. The total deflection is modeled as a superposition of bending in two orthogonal planes. For B_i these planes are the $\underline{i}_1 - \underline{i}_2$ plane and $\underline{i}_1 - \underline{i}_3$ planes. The deflection is modeled with the assumed modes method [49], which involves the deflection at point x along the boom B_i at time t to be computed as

$$\mathbf{u}^i(x, t) = \begin{bmatrix} u_2^i(x, t) \\ u_3^i(x, t) \end{bmatrix} = \boldsymbol{\Psi}(x) \mathbf{q}^{\epsilon i}(t), \quad (6)$$

where $u_2^i(x, t)$ and $u_3^i(x, t)$ are the elastic deformations at a distance x along the boom (i.e., in the \underline{i}_1 axis) in the \underline{i}_2 and \underline{i}_3 axes, respectively;

$$\boldsymbol{\Psi}(x) = \begin{bmatrix} \boldsymbol{\Psi}_{u_2}(x) \\ \boldsymbol{\Psi}_{u_3}(x) \end{bmatrix} = \begin{bmatrix} \Psi_1(x) & \Psi_2(x) & \dots & \Psi_n(x) & 0 & 0 & \dots & 0 \\ 0 & 0 & \dots & 0 & \Psi_1(x) & \Psi_2(x) & \dots & \Psi_n(x) \end{bmatrix}$$

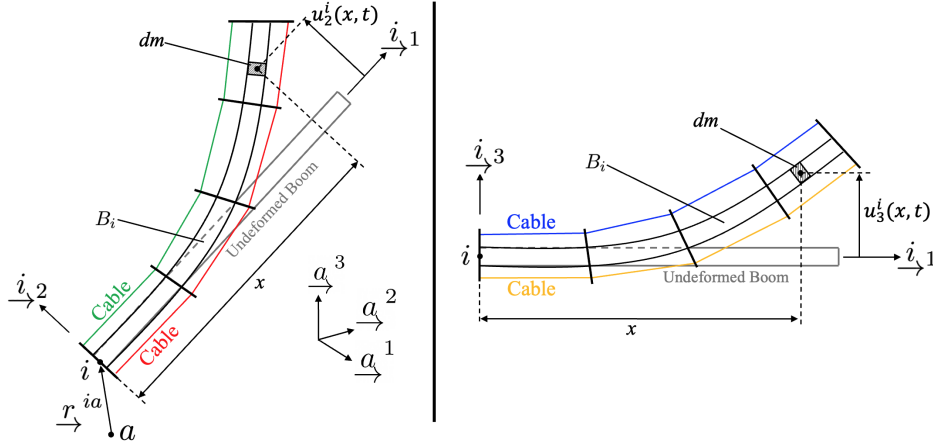


Fig. 16 Boom component, B_i , with deflection $u_1^i(x, t)$ and $u_2^i(x, t)$ in two perpendicular planes shown with the actuation cables.

contains the n chosen basis functions repeated in each orthogonal direction; and $\mathbf{q}^{\epsilon i}$ is a column vector containing the $2n$ elastic coordinates of B_i . The basis functions must be twice differentiable and satisfy the boundary conditions $\frac{\partial \Psi_i(x)}{\partial x}|_{x=0} = 0$ and $\frac{\partial^2 \Psi_i(x)}{\partial x^2}|_{x=0} = 0$ to match the root condition of a cantilevered beam. The three following basis functions are chosen for this preliminary work, $\Psi_1(x) = x^2$, $\Psi_1(x) = x^3$, and $\Psi_1(x) = x^4$. Any number of functions obeying the aforementioned boundary conditions may be selected, so $\Psi(x)$ will be used to preserve generality.

The generalized coordinates for the unconstrained boom component B_i are $\mathbf{q}^{B_i} = \begin{bmatrix} \mathbf{r}_a^{ia\top} & \mathbf{p}^{ia\top} & \mathbf{q}^{\epsilon i\top} \end{bmatrix}$, where \mathbf{p}^{ia} is the vectorized DCM \mathbf{C}_{ia} , \mathbf{r}_a^{ia} is the position of the base of the boom with respect to an unforced particle a resolved in inertial frame \mathcal{F}_a , and $\mathbf{q}^{\epsilon i}$ is the elastic coordinates of B_i . The generalized velocities for the unconstrained boom component B_i , where $i \in \{c, d, e, f\}$ are $\mathbf{v}^{B_i} = \begin{bmatrix} \mathbf{r}_a^{ia\top} & \boldsymbol{\omega}_i^{ia\top} & \dot{\mathbf{q}}^{\epsilon i\top} \end{bmatrix}$, where $\boldsymbol{\omega}_i^{ia}$ is the angular velocity vector of boom body frame \mathcal{F}_i relative to \mathcal{F}_a , resolved in \mathcal{F}_i . These generalized velocities are related to the generalized coordinates through the mappings

$$\dot{\mathbf{q}}^{B_i} = \Gamma_{B_i} \mathbf{v}^{B_i}, \quad (7)$$

$$\mathbf{v}^{B_i} = \mathbf{S}_{B_i} \dot{\mathbf{q}}^{B_i}, \quad (8)$$

where $\Gamma_{B_i} = \text{diag}\{\mathbf{1}, \Gamma_i^{ia}(\mathbf{p}^{ia}), \mathbf{1}\}$, $\mathbf{S}_{B_i} = \text{diag}\{\mathbf{1}, \mathbf{S}_i^{ia}(\mathbf{p}^{ia}), \mathbf{1}\}$, and $\mathbf{S}_{B_i} \Gamma_{B_i} = \mathbf{1}$.

The deformed position of a mass element dm at length x along boom B_i relative to point a and resolved in \mathcal{F}_a is given by

$$\mathbf{r}_a^{dma} = \mathbf{r}_a^{ia} + \mathbf{C}_{ia}^\top \mathbf{r}_i^{dmi},$$

where $\mathbf{r}_i^{dmi\top} = \begin{bmatrix} x & \mathbf{u}^{i\top}(x, t) \end{bmatrix} = \begin{bmatrix} x & (\Psi(x)\mathbf{q}^{\epsilon i}(t))^\top \end{bmatrix}$.

IX. Component Kinetic & Potential Energies

Kinetic energy is modeled for all components with the respective generalized velocities. It is assumed that all components exist outside of any gravity field, so potential energy is only modeled for the CABLESSail boom components in the form of strain energy.

A. Solar Sail Bus

The kinetic energy of the Solar sail bus, body B_b , is

$$T_{B_b a/a} = \frac{1}{2} m_{B_b} \dot{\mathbf{r}}_a^{ba\top} \dot{\mathbf{r}}_a^{ba} + \frac{1}{2} \omega_b^{ba\top} \mathbf{I}_b^{B_b b} \omega_b^{ba} = \frac{1}{2} \mathbf{v}^{B_b\top} \mathbf{M}_{B_b} \mathbf{v}^{B_b} = \frac{1}{2} \dot{\mathbf{q}}^{B_b\top} \mathbf{S}_{B_b}^\top \mathbf{M}_{B_b} \mathbf{S}_{B_b} \dot{\mathbf{q}}^{B_b}, \quad (9)$$

where m_{B_b} is the mass of body B_b , $\mathbf{I}_b^{B_b b}$ is the moment of inertia matrix of body B_b relative to point b resolved in \mathcal{F}_b , and the mass matrix is given by $\mathbf{M}_{B_b} = \text{diag}\{m_{B_b}, \mathbf{1}, \mathbf{I}_b^{B_b b}\}$.

B. Spacecraft Bus

The kinetic energy of the spacecraft bus, body B_g , are derived similarly to the solar sail bus, resulting in

$$T_{B_g a/a} = \frac{1}{2} m_{B_g} \dot{\mathbf{r}}_a^{ga\top} \dot{\mathbf{r}}_a^{ga} + \frac{1}{2} \omega_g^{ga\top} \mathbf{I}_g^{B_g g} \omega_g^{ga} = \frac{1}{2} \mathbf{v}^{B_g\top} \mathbf{M}_{B_g} \mathbf{v}^{B_g} = \frac{1}{2} \dot{\mathbf{q}}^{B_g\top} \mathbf{S}_{B_g}^\top \mathbf{M}_{B_g} \mathbf{S}_{B_g} \dot{\mathbf{q}}^{B_g}, \quad (10)$$

where m_{B_g} is the mass of body B_g , $\mathbf{I}_g^{B_g g}$ is the moment of inertia matrix of body B_g relative to point g resolved in \mathcal{F}_g , and the mass matrix is given by $\mathbf{M}_{B_g} = \text{diag}\{m_{B_g}, \mathbf{1}, \mathbf{I}_g^{B_g g}\}$.

C. CABLESSail Booms

The flexible boom is modeled as an Euler-Bernoulli beam and therefore has a strain energy due to bending in its two transverse directions given by [49]

$$V_{B_i} = \frac{1}{2} EI \int_0^L \left[\left(\frac{\partial^2 u_2(x)}{\partial x^2} \right)^2 + \left(\frac{\partial^2 u_3(x)}{\partial x^2} \right)^2 \right] dx, \quad (11)$$

where E is the modulus of elasticity of the boom and I is the second moment of area of the boom cross section. Using the deflection definition in (6), the strain energy of body B_i

$$V_{B_i} = \frac{1}{2} \mathbf{q}^{\epsilon i\top} \left(EI \int_0^L \left(\frac{\partial^2 \Psi}{\partial x^2} \right)^\top \left(\frac{\partial^2 \Psi}{\partial x^2} \right) dx \right) \mathbf{q}^{\epsilon i} = \frac{1}{2} \mathbf{q}^{B_i\top} \mathbf{K}_{B_i} \mathbf{q}^{B_i}, \quad (12)$$

where $\mathbf{K}_{B_i} = \text{diag} \left\{ \mathbf{0}, \mathbf{0}, EI \int_0^L \left(\frac{\partial^2 \Psi}{\partial x^2} \right)^\top \left(\frac{\partial^2 \Psi}{\partial x^2} \right) dx \right\}$.

The kinetic energy of the boom B_i is the integral along the boom of the kinetic energy of every mass element, dm ,

and is computed as

$$T_{B_i a/a} = \frac{1}{2} \int_{\mathcal{B}} \underline{r}^{dma^a} \cdot \underline{r}^{dma^a} dm = \frac{1}{2} \int_{\mathcal{B}} \underline{v}^{dma/a} \cdot \underline{v}^{dma/a} dm, \quad (13)$$

where $\underline{r}^{dma} = \underline{r}^{dmi} + \underline{r}^{ia}$. Note that \underline{r}^{ia} is the location of the base of the boom B_i relative to point a and \underline{r}^{dmi} is the location of the mass element relative to the base of the boom. The deflections are used to define the mass element position, where $\mathbf{r}_i^{dmi^T} = \left[x \quad (\Psi(x)\mathbf{q}^{\epsilon i})^T \right]$. After taking the time derivative of \underline{r}^{dma} with respect to \mathcal{F}_a , the kinetic energy of the boom can be factored into the quadratic form

$$T_{B_i w/a} = \frac{1}{2} \mathbf{v}^{B_i^T} \mathbf{M}_{B_i} \mathbf{v}^{B_i}, \quad (14)$$

where the mass matrix \mathbf{M}_{B_i} is given by

$$\mathbf{M}_{B_i} = \begin{bmatrix} m_{B_i} \mathbf{I} & -\mathbf{C}_{ia}^T \mathbf{c}_i^{B_i i^\times} & \mathbf{C}_{ia}^T \mathbf{H}_{B_i} \\ -\mathbf{c}_i^{B_i i^\times T} \mathbf{C}_{ia} & \mathbf{I}_i^{B_i i} & -\mathbf{G}_{B_i} \\ \mathbf{H}_{B_i}^T \mathbf{C}_{ia} & -\mathbf{G}_{B_i}^T & \mathbf{P}_{B_i} \end{bmatrix}. \quad (15)$$

The contents of the mass matrix include the boom's total mass, m_{B_i} , the boom's first moment of mass relative to point i resolved in \mathcal{F}_i , $\mathbf{c}_i^{B_i i}$, the boom's second moment of mass relative to point i resolved in \mathcal{F}_i , $\mathbf{I}_i^{B_i i}$, and other matrices associated with the elastic coordinates, \mathbf{H}_{B_i} , \mathbf{G}_{B_i} , and \mathbf{P}_{B_i} . Detailed derivations of these terms are found in Appendix A of [41], where it is also shown that the time derivative of \mathbf{M}_{B_i} is

$$\dot{\mathbf{M}}_{B_i} = \begin{bmatrix} \mathbf{0} & (\omega_i^{ia^\times} \mathbf{C}_{ia})^T \mathbf{c}_i^{B_i i^\times} & -(\omega_i^{ia^\times} \mathbf{C}_{ia})^T \mathbf{H}_{B_i} \\ \mathbf{c}_i^{B_i i^\times T} \omega_i^{ia^\times} \mathbf{C}_{ia} & \mathbf{0} & \mathbf{0} \\ -\mathbf{H}_{B_i}^T \omega_i^{ia^\times} \mathbf{C}_{ia} & \mathbf{0} & \mathbf{0} \end{bmatrix}. \quad (16)$$

To assist with the derivation of the boom's equations of motion, it is convenient to substitute the kinematic mapping (8) into (14), resulting in the kinetic energy expression

$$T_{B_i a/a} = \frac{1}{2} \dot{\mathbf{q}}^{B_i^T} \mathbf{S}_{B_i}^T \mathbf{M}_{B_i} \mathbf{S}_{B_i} \dot{\mathbf{q}}^{B_i}. \quad (17)$$

X. Component Generalized Forces

External forces that do work on the system are considered with the null-space method. Thus, the SRP force and torque are considered for the solar sail bus, and the reaction forces due to cable tensioning are considered for the booms.

No other forces are considered for this work, but the methods presented here may easily be adapted for other applications.

A. Solar Sail Bus

The solar sail membrane detailed in Section III.C produces an external force and torque pair that is applied at the center of mass of the solar sail bus, which is assumed to be coincident with the center of the solar sail membrane if it were perfectly flat with undeformed booms. To preserve generality, a generic external force is considered.

The virtual work done by the external force \vec{f}^{B_b} acting on the center of mass of the solar sail bus is

$$\delta W^{B_b f} = \vec{f}^{B_b} \cdot \vec{r}^{ba} = \mathbf{f}_a^{B_b \top} \delta \mathbf{r}_a^{ba} = \mathbf{f}_b^{B_b \top} \mathbf{C}_{ba} \delta \mathbf{r}_a^{ba} = \delta \mathbf{q}^{B_i \top} \begin{bmatrix} \mathbf{C}_{ba}^\top \mathbf{f}_b^{B_b} \\ \mathbf{0} \end{bmatrix}, \quad (18)$$

where $\mathbf{f}_b^{B_b}$ contains the components of \vec{f}^{B_b} resolved in \mathcal{F}_b .

The virtual work done by the external torque $\vec{\tau}^{B_b}$ acting on the solar sail bus is

$$\delta W^{B_b \tau} = \tau_b^{B_b \top} \delta \theta, \quad (19)$$

where

$$\delta \theta = \frac{\partial \omega_b^{ba}}{\partial \dot{\mathbf{p}}^{ba}} \delta \mathbf{p}^{ba} = \frac{\partial}{\partial \dot{\mathbf{p}}^{ba}} \left(\mathbf{S}(\mathbf{p}^{ba}) \dot{\mathbf{p}}^{ba} \right) \delta \mathbf{p}^{ba} = \mathbf{S}(\mathbf{p}^{ba}) \delta \mathbf{p}^{ba}. \quad (20)$$

Substituting (20) into (19) results in

$$\delta W^{B_b \tau} = \tau_b^{B_b \top} \mathbf{S}(\mathbf{p}^{ba}) \delta \mathbf{p}^{ba} = \delta \mathbf{q}^{B_i \top} \begin{bmatrix} \mathbf{0} \\ \mathbf{S}^\top(\mathbf{p}^{ba}) \tau_b^{B_b} \end{bmatrix}. \quad (21)$$

Combining the results from (18) and (21), the generalized forces acting on B_b due to the external force and torque are

$$\mathbf{f}_{B_i} = \begin{bmatrix} \mathbf{C}_{ba}^\top \mathbf{f}_b^{B_b} \\ \mathbf{S}^\top(\mathbf{p}^{ba}) \tau_b^{B_b} \end{bmatrix}.$$

B. CABLESSail Booms

Each of the booms, denoted by bodies B_i , $i \in \{c, d, e, f\}$, have actuating cables routed through them, as shown in Fig. 16. When tension is applied to the cables, they impart reaction forces on the boom, which then results in bending of the boom. To provide full actuation capabilities in each of the bending directions, four cables are included: one along the ‘‘top’’ of the boom (nominally a distance $R + h$ in the positive \underline{i}_3 from the boom’s neutral axis), one along the

“bottom” of the boom (nominally a distance $R + h$ in the negative \underline{i}_3 from the boom’s neutral axis), as well as cables along the “sides” of the boom (nominally distances $R + h$ in the positive and negative \underline{i}_2 from the boom’s neutral axis). The j^{th} cable, $j \in \{1, 2, 3, 4\}$ passes through routing holes located at points $l_{j,k}$, $k = 1, \dots, n - 1$ and is attached to the end of the boom at the point $l_{j,n}$. The position of points $l_{j,k}$ relative to point i at the root of the boom is given by

$$\mathbf{r}_i^{l_{j,k}i} = \mathbf{r}_r^{p_ki} + \mathbf{C}_{p_ki}^\top \mathbf{r}_{p_k}^{l_{j,k}p_k}, \quad (22)$$

where $\mathbf{r}_r^{p_ki} = [x_k \ \Psi(x_k) \mathbf{q}^{\epsilon i}]$ is the deformed position of the beam at the spreader routing hole a distance x_k down the length of the boom, $\mathbf{C}_{p_ki} \approx \mathbf{1} - \theta^{p_ki \times}$ is the small angle approximation of the deformed attitude of the boom at a length x_k down its length with $\theta^{p_ki} = \left[0 \ -\left(\frac{\partial \Psi_{u_3}}{\partial x} \mathbf{q}^{\epsilon i}\right)^\top \ \left(\frac{\partial \Psi_{u_2}}{\partial x} \mathbf{q}^{\epsilon i}\right)^\top \right]$ [39, 50], and $\mathbf{r}_{p_k}^{l_{j,k}p_k}$ is the position of the cable routing point relative to the deformed point p_k with

$$\mathbf{r}_{p_k}^{l_{1,k}p_k} = \begin{bmatrix} 0 & 0 & R + h \end{bmatrix}, \quad \mathbf{r}_{p_k}^{l_{2,k}p_k} = \begin{bmatrix} 0 & 0 & -(R + h) \end{bmatrix}, \quad \mathbf{r}_{p_k}^{l_{3,k}p_k} = \begin{bmatrix} 0 & R + h & 0 \end{bmatrix}, \quad \mathbf{r}_{p_k}^{l_{4,k}p_k} = \begin{bmatrix} 0 & -(R + h) & 0 \end{bmatrix}.$$

In this note, it is assumed that the spreaders are equally spaced along the length of the boom, such that $\Delta x = x_{k+1} - x_k$, $k = 1, \dots, n - 1$ is a constant distance.

It is assumed that there is no friction between the cable surface and the routing hole in the spreader plate, so the only reaction forces are perpendicular to the deflected boom. The reaction force for the j^{th} cable at location $l_{j,k}$ is

$$\mathbf{f}_i^{Bif_{j,k}} = \frac{T_j}{\Delta x} \left(\mathbf{r}_i^{l_{j,k+1}i} - 2\mathbf{r}_i^{l_{j,k}i} + \mathbf{r}_i^{l_{j,k-1}i} \right), \quad j = 1, 2, 3, 4, \quad k = 1, \dots, n - 1,$$

where T_j is the tension within the j^{th} cable and $x_0 = 0$. The reaction force due to the j^{th} cable at the end of the boom is given by

$$\mathbf{f}_i^{Bif_{j,n}} = \frac{T_j}{\Delta x} \left(\mathbf{r}_i^{l_{j,n}i} - \mathbf{r}_i^{l_{j,n-1}i} \right), \quad j = 1, 2, 3, 4.$$

The cable reaction force $\vec{f}^{Bif_{j,k}}$ is applied at point $l_{j,k}$ whose position relative to point a resolved in \mathcal{F}_a is

$$\mathbf{r}_a^{l_{j,k}a} = \mathbf{r}_a^{ia} + \mathbf{C}_{ia}^\top \mathbf{r}_r^{p_ki} + \mathbf{C}_{ia}^\top \mathbf{C}_{p_ki}^\top \mathbf{r}_{p_k}^{l_{j,k}p_k}. \quad (23)$$

The virtual work done by $\vec{f}^{Bif_{j,k}}$ is

$$\delta W^{Bif_{j,k}} = \vec{f}^{Bif_{j,k}} \cdot \delta \vec{r}^{l_{j,k}a} = \mathbf{f}_a^{Bif_{j,k}^\top} \delta \mathbf{r}_a^{l_{j,k}a} = \mathbf{f}_i^{Bif_{j,k}^\top} \mathbf{C}_{ia} \delta \mathbf{r}_a^{l_{j,k}a}. \quad (24)$$

The computation of the virtual displacement $\delta \mathbf{r}_a^{l_{j,k}a}$ is described in Appendix B of [41], where it is shown that (24) is

related to a virtual displacement in the generalized coordinates through the equation

$$\delta W^{B_i f_{j,k}} = \delta \mathbf{q}^{B_i T} \left[\begin{array}{c} \mathbf{C}_{ia}^T \mathbf{f}_i^{B_i f_{j,k}} \\ \left(\frac{\partial}{\partial \mathbf{p}^{ia}} \left(\mathbf{C}_{ia}^T \left(\mathbf{r}_i^{pki} + \mathbf{C}_{pki}^T \mathbf{r}_l^{l_{j,k} p k} \right) \right) \right)^T \mathbf{C}_{ia}^T \mathbf{f}_i^{B_i f_{j,k}} \\ \left(\left[\begin{array}{c} \mathbf{0} \\ \Psi(x_k) \end{array} \right]^T + \left[\begin{array}{c} \mathbf{0} \\ -\frac{\partial \Psi_{u_3}}{\partial x} \\ \frac{\partial \Psi_{u_2}}{\partial x} \end{array} \right]^T \mathbf{r}_{p_k}^{l_{j,k} p k \times} \right) \mathbf{f}_i^{B_i f_{j,k}} \end{array} \right].$$

Therefore the generalized forces due to the cable reaction forces on body B_i are

$$\mathbf{f}_{B_i} = \sum_{j=1}^4 \sum_{k=0}^n \left[\begin{array}{c} \mathbf{C}_{ia}^T \mathbf{f}_i^{B_i f_{j,k}} \\ \left(\frac{\partial}{\partial \mathbf{p}^{ia}} \left(\mathbf{C}_{ia}^T \left(\mathbf{r}_i^{pki} + \mathbf{C}_{l_{ki}}^T \mathbf{r}_l^{l_{k} p k} \right) \right) \right)^T \mathbf{C}_{ia}^T \mathbf{f}_i^{B_i f_{j,k}} \\ \left(\left[\begin{array}{c} \mathbf{0} \\ \Psi(x_k) \end{array} \right]^T + \left[\begin{array}{c} \mathbf{0} \\ -\frac{\partial \Psi_{u_3}}{\partial x} \\ \frac{\partial \Psi_{u_2}}{\partial x} \end{array} \right]^T \mathbf{r}_l^{l_{k} p k \times} \right) \mathbf{f}_i^{B_i f_{j,k}} \end{array} \right].$$

XI. Lagrange's Equations for Each Component

Lagrange's equation is used to derive the equations of motion for each component. The general form of Lagrange's equation is given as

$$\frac{d}{dt} \left(\frac{\partial L}{\partial \dot{\mathbf{q}}} \right)^T - \left(\frac{\partial L}{\partial \mathbf{q}} \right)^T = \mathbf{f} + \Xi^T \lambda, \quad (25)$$

where $L = T - V$ is the Lagrangian, T is the kinetic energy, V is the potential energy, \mathbf{q} contains the generalized coordinates, \mathbf{f} is the generalized forces, Ξ is the constraint matrix associated with the constraints $\Xi \mathbf{q} = \mathbf{0}$, and λ are Lagrange multipliers.

A. CABLESSail Booms

For boom body B_i , the Lagrangian is $L_{B_i a/a} = T_{B_i a/a} - V_{B_i}$, \mathbf{q}^{B_i} are the generalized coordinates, \mathbf{f}_{B_i} are the generalized forces, Ξ_{B_i} is the constraint matrix associated with the constrained attitude parameters, and λ_{B_i} are Lagrange multipliers. Since the potential energy does not depend on the generalized velocities, Lagrange's equation for body B_i can then be written as

$$\frac{d}{dt} \left(\frac{\partial T_{B_i a/a}}{\partial \dot{\mathbf{q}}^{B_i}} \right)^T - \left(\frac{\partial T_{B_i a/a}}{\partial \mathbf{q}^{B_i}} \right)^T + \left(\frac{\partial V_{B_i}}{\partial \mathbf{q}^{B_i}} \right)^T = \mathbf{f}_{B_i} + \Xi_{B_i} \lambda_{B_i}. \quad (26)$$

The partial derivatives of the boom's kinetic and potential energy are solved using the expressions in (12) and (17), resulting in

$$\begin{aligned} & \frac{d}{dt} \left(\frac{\partial T_{B_i a/a}}{\partial \dot{\mathbf{q}}^{B_i}} \right)^\top - \left(\frac{\partial T_{B_i a/a}}{\partial \mathbf{q}^{B_i}} \right)^\top + \left(\frac{\partial V_{B_i}}{\partial \mathbf{q}^{B_i}} \right)^\top \\ &= \mathbf{S}_{B_i}^\top \mathbf{M}_{B_i} \dot{\mathbf{v}}^{B_i} + \mathbf{S}_{B_i}^\top \dot{\mathbf{M}}_{B_i} \mathbf{v}^{B_i} + \left(\dot{\mathbf{S}}_{B_i}^\top - \hat{\boldsymbol{\Omega}}_{B_i} \right) \mathbf{M}_{B_i} \mathbf{v}^{B_i} - \begin{bmatrix} \mathbf{0} \\ \left(\frac{\hat{\partial}(\mathbf{C}_{ia}^\top \mathbf{v}^{B_i})}{\hat{\partial} \mathbf{p}^{ia}} \right)^\top \dot{\mathbf{r}}_a^{ia} \\ \mathbf{0} \end{bmatrix} + \mathbf{K}_{B_i} \mathbf{q}^{B_i}, \end{aligned} \quad (27)$$

where $\hat{\boldsymbol{\Omega}}_{B_i} = \text{diag} \left\{ \mathbf{0}, \left(\frac{\partial \omega_i^{ia}}{\partial \mathbf{p}^{ia}} \right)^\top, \mathbf{0} \right\}$, $\mathbf{v}^{B_i} = \mathbf{H}_{B_i} \dot{\mathbf{q}}^{\epsilon_i} - \mathbf{c}_i^{B_i \times} \omega_i^{ia}$, and $\frac{\hat{\partial}(\mathbf{C}_{ia}^\top \mathbf{v}^{B_i})}{\hat{\partial} \mathbf{p}^{ia}}$ is the partial derivative of $\mathbf{C}_{ia}^\top \mathbf{v}^{B_i}$ with respect to \mathbf{p}^{ia} considering \mathbf{v}^{B_i} as a constant. Details regarding the computation of these partial derivatives are provided in Appendix C of [41].

B. Solar Sail Bus

The Lagrangian of the rigid hub B_b is $L_{B_b a/a} = T_{B_b a/a}$, its generalized coordinates are \mathbf{q}^{B_b} , resulting in Lagrange's equation for body B_b in the form

$$\frac{d}{dt} \left(\frac{\partial T_{B_b a/a}}{\partial \dot{\mathbf{q}}^{B_b}} \right)^\top - \left(\frac{\partial T_{B_b a/a}}{\partial \mathbf{q}^{B_b}} \right)^\top = \mathbf{f}_{B_b} + \boldsymbol{\Xi}_{B_b} \boldsymbol{\lambda}_{B_b}. \quad (28)$$

A similar procedure to that used for the CABLESSail booms is performed on the spacecraft hub's kinetic energy in (9), which results in

$$\frac{d}{dt} \left(\frac{\partial T_{B_b a/a}}{\partial \dot{\mathbf{q}}^{B_b}} \right)^\top - \left(\frac{\partial T_{B_b a/a}}{\partial \mathbf{q}^{B_b}} \right)^\top = \mathbf{S}_{B_b}^\top \mathbf{M}_{B_b} \dot{\mathbf{v}}^{B_b} + \mathbf{S}_{B_b}^\top \dot{\mathbf{M}}_{B_b} \mathbf{v}^{B_b} + \left(\dot{\mathbf{S}}_{B_b}^\top - \hat{\boldsymbol{\Omega}}_{B_b} \right) \mathbf{M}_{B_b} \mathbf{v}^{B_b}, \quad (29)$$

where $\hat{\boldsymbol{\Omega}}_{B_b} = \text{diag} \left\{ \mathbf{0}, \left(\frac{\partial \omega_b^{ba}}{\partial \mathbf{p}^{ba}} \right)^\top \right\}$. Details of this computation are also provided in Appendix C of [41].

C. Spacecraft Bus

The equations of motion of both buses are identical up to specific dimension and inertia values. Therefore the resulting Lagrange's equation of motion for the spacecraft bus, B_g , are nearly identical to (29), resulting in

$$\frac{d}{dt} \left(\frac{\partial T_{B_g a/a}}{\partial \dot{\mathbf{q}}^{B_g}} \right)^\top - \left(\frac{\partial T_{B_g a/a}}{\partial \mathbf{q}^{B_g}} \right)^\top = \mathbf{S}_{B_g}^\top \mathbf{M}_{B_g} \dot{\mathbf{v}}^{B_g} + \mathbf{S}_{B_g}^\top \dot{\mathbf{M}}_{B_g} \mathbf{v}^{B_g} + \left(\dot{\mathbf{S}}_{B_g}^\top - \hat{\boldsymbol{\Omega}}_{B_g} \right) \mathbf{M}_{B_g} \mathbf{v}^{B_g}, \quad (30)$$

XII. Attitude Parameterization Constraint

To ensure a valid attitude parameterization, the vectorized DCM associated with each of the components must be constrained through the Lagrange multipliers λ_i , $i \in \{b, c, d, e, f, g\}$. As shown in [48], the orthonormal property of the DCM results in its vectorized parameters satisfying the constraints

$$\Phi(\mathbf{p}^{ia}) = \begin{bmatrix} \mathbf{p}_1^{ia\top} \mathbf{p}_1^{ia} - 1 \\ \mathbf{p}_2^{ia\top} \mathbf{p}_2^{ia} - 1 \\ \mathbf{p}_1^{ia\top} \mathbf{p}_2^{ia} \\ \mathbf{p}_1^{ia\times} \mathbf{p}_2^{ia} - \mathbf{p}_3^{ia} \end{bmatrix} = \mathbf{0},$$

which can alternatively be written at the rate level as

$$\Xi_i^{ia} \dot{\mathbf{p}}^{ia} = \mathbf{0}, \quad (31)$$

where

$$\Xi_i^{ia} = \begin{bmatrix} \mathbf{p}_1^{ia\top} & \mathbf{0} & \mathbf{0} \\ \mathbf{0} & \mathbf{p}_2^{ia\top} & \mathbf{0} \\ \mathbf{p}_2^{ia\top} & \mathbf{p}_1^{ia\top} & \mathbf{0} \\ -\mathbf{p}_2^{ia\times} & \mathbf{p}_1^{ia\times} & -\mathbf{1} \end{bmatrix}. \quad (32)$$

The constraint matrix in (32) is related to the constraint matrices in (26) and (28) through the relationships

$$\Xi_{B_i} = \begin{bmatrix} \mathbf{0} & \Xi_i^{ia} & \mathbf{0} \end{bmatrix}, \quad i \in \{c, d, e, f\}, \quad (33)$$

$$\Xi_{B_b} = \begin{bmatrix} \mathbf{0} & \Xi_b^{ba} \end{bmatrix}, \quad (34)$$

which allows for (31) to be rewritten as

$$\Xi_{B_i} \dot{\mathbf{q}}^{B_i} = \mathbf{0}, \quad i \in \{c, d, e, f\}, \quad (35)$$

$$\Xi_{B_b} \dot{\mathbf{q}}^{B_b} = \mathbf{0}. \quad (36)$$

Substituting (4) and (7) into (35) and (36), respectively, results in the properties $\Xi_{B_i} \mathbf{\Gamma}_{B_i} = \mathbf{0}$, $i \in \{c, d, e, f\}$ and $\Xi_{B_b} \mathbf{\Gamma}_{B_b} = \mathbf{0}$. This demonstrates how $\mathbf{\Gamma}_{B_i}$ and $\mathbf{\Gamma}_{B_b}$ lie in the nullspace of the constraint matrices, which forms the basis of the null-space constraint technique.

The method proceeds for the boom equations of motion by substituting (27) into (26), then pre-multiplying on the left by $\Gamma_{B_i}^\top$, resulting in

$$\begin{aligned} \Gamma_{B_i}^\top \mathbf{S}_{B_i}^\top \mathbf{M}_{B_i} \dot{\mathbf{v}}^{B_i} + \Gamma_{B_i}^\top \mathbf{S}_{B_i}^\top \dot{\mathbf{M}}_{B_i} \mathbf{v}^{B_i} + \Gamma_{B_i}^\top \left(\dot{\mathbf{S}}_{B_i}^\top - \hat{\boldsymbol{\Omega}}_{B_i} \right) \mathbf{M}_{B_i} \mathbf{v}^{B_i} - \Gamma_{B_i}^\top \begin{bmatrix} \mathbf{0} \\ \left(\frac{\hat{\partial}(\mathbf{C}_{ia}^\top \mathbf{v}^{B_i})}{\hat{\partial} \mathbf{p}^{ia}} \right)^\top \mathbf{r}_a^{ia} \\ \mathbf{0} \end{bmatrix} + \Gamma_{B_i}^\top \mathbf{K}_{B_i} \mathbf{q}^{B_i} \\ = \Gamma_{B_i}^\top \mathbf{f}_{B_i} + \Gamma_{B_i}^\top \boldsymbol{\Xi}_{B_i}^\top \boldsymbol{\lambda}_{B_i}. \end{aligned} \quad (37)$$

We know that $\Gamma_{B_i} \mathbf{S}_{B_i} = \Gamma_{B_i}^\top \mathbf{S}_{B_i}^\top = \mathbf{1}$ and $\Gamma_{B_i}^\top \boldsymbol{\Xi}_{B_i}^\top = \mathbf{0}$, therefore, (37) is simplified to

$$\mathbf{M}_{B_i} \dot{\mathbf{v}}^{B_i} + \dot{\mathbf{M}}_{B_i} \mathbf{v}^{B_i} + \Gamma_{B_i}^\top \left(\dot{\mathbf{S}}_{B_i}^\top - \hat{\boldsymbol{\Omega}}_{B_i} \right) \mathbf{M}_{B_i} \mathbf{v}^{B_i} - \Gamma_{B_i}^\top \begin{bmatrix} \mathbf{0} \\ \left(\frac{\hat{\partial}(\mathbf{C}_{ia}^\top \mathbf{v}^{B_i})}{\hat{\partial} \mathbf{p}^{ia}} \right)^\top \mathbf{r}_a^{ia} \\ \mathbf{0} \end{bmatrix} + \Gamma_{B_i}^\top \mathbf{K}_{B_i} \mathbf{q}^{B_i} = \Gamma_{B_i}^\top \mathbf{f}_{B_i}. \quad (38)$$

As a final step in the derivation of these equations of motion, the identities $\Gamma_{B_i}^\top \left(\dot{\mathbf{S}}_{B_i}^\top - \hat{\boldsymbol{\Omega}}_{B_i} \right) = \boldsymbol{\Omega}_{B_i}$ and $\Gamma_i^{ia^\top} \left(\frac{\hat{\partial}(\mathbf{C}_{ia}^\top \mathbf{v}^{B_i})}{\hat{\partial} \mathbf{p}^{ia}} \right)^\top = \mathbf{v}_i^{B_i^\times} \mathbf{C}_{ia}$ from [48] are made use of, where $\boldsymbol{\Omega}_{B_i} = \text{diag}\{\mathbf{0}, \omega_i^{ia^\times}, \mathbf{0}\}$. Applying these identities to (38) results in

$$\mathbf{M}_{B_i} \dot{\mathbf{v}}^{B_i} + \Gamma_{B_i}^\top \mathbf{K}_{B_i} \mathbf{q}^{B_i} + \mathbf{f}_{B_i}^{non} = \Gamma_{B_i}^\top \mathbf{f}_{B_i}, \quad i \in \{d, e, f, g\}, \quad (39)$$

where $\mathbf{f}_{B_i}^{non} = (\dot{\mathbf{M}}_{B_i} + \boldsymbol{\Omega}_{B_i} \mathbf{M}_{B_i}) \mathbf{v}^{B_i} - \left[\mathbf{0} \quad \left(\mathbf{v}_i^{B_i^\times} \mathbf{C}_{ia} \mathbf{r}_a^{ia} \right)^\top \quad \mathbf{0} \right]^\top$. The equations of motion of boom body $B_i, i \in \{c, d, e, f\}$ with the Lagrange multipliers removed are thus given by (39).

A similar process is used to obtain the equations of motion for both the solar sail and spacecraft buses, bodies B_b, B_c , in the form

$$\mathbf{M}_{B_i} \dot{\mathbf{v}}^{B_i} + \mathbf{f}_{B_i}^{non} = \Gamma_{B_i}^\top \mathbf{f}_{B_i}, \quad i \in \{b, g\}, \quad (40)$$

where $\mathbf{f}_{B_b}^{non} = (\dot{\mathbf{M}}_{B_b} + \boldsymbol{\Omega}_{B_b} \mathbf{M}_{B_b}) \mathbf{v}^{B_b}$ and $\boldsymbol{\Omega}_{B_b} = \text{diag}\{\mathbf{0}, \omega_b^{ba^\times}\}$.

XIII. Modular Multi-body Dynamic Modeling

With the dynamics of each individual component fully described in (39) and (40) with the attitude parameterization Lagrange multipliers removed, the components can now be constrained together to ‘‘assemble’’ the full solar sail. First, all independent component equations of motion are aggregated into a single matrix expression. Then, the assembly constraints are defined and enforced, followed by the application of the null-space method to remove the corresponding

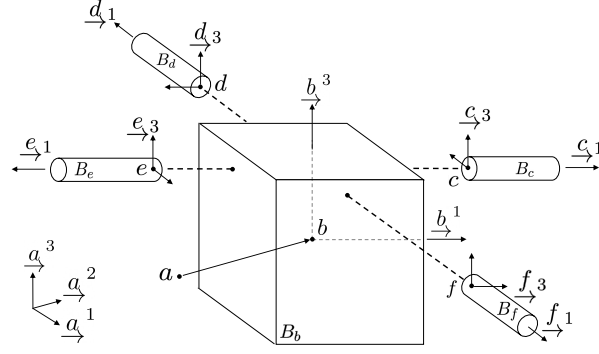


Fig. 17 Exploded view of CABLESSail Assembly #1 consisting of solar sail bus B_b , and CABLESSail booms B_c - B_f , shortened for clarity, with corresponding body frames and attachment points.

Lagrange multipliers. This process is first shown in detail for a nominal assembly of CABLESSail, then an abbreviated description is given for a second assembly where the optional spacecraft bus is used to represent an active mass translator actuator.

A. Aggregate Component Equations of Motion

The unconstrained dynamics for each individual component are gathered into a single set of equations to fully represent the system of unassembled components. The generalized coordinates of this aggregate system are $\mathbf{q}^\top = [\mathbf{q}^{B_b^\top} \ \mathbf{q}^{B_c^\top} \ \mathbf{q}^{B_d^\top} \ \mathbf{q}^{B_e^\top} \ \mathbf{q}^{B_f^\top}]$, while the generalized velocities of the aggregate system are $\mathbf{v}^\top = [\mathbf{v}^{B_b^\top} \ \mathbf{v}^{B_c^\top} \ \mathbf{v}^{B_d^\top} \ \mathbf{v}^{B_e^\top} \ \mathbf{v}^{B_f^\top}]$. The unconstrained dynamics of the components are written in an aggregate form as

$$\mathbf{M}\dot{\mathbf{v}} + \mathbf{\Gamma}^\top \mathbf{K}\mathbf{q} + \mathbf{f}^{non} = \mathbf{\Gamma}^\top \mathbf{f}, \quad (41)$$

where the aggregate matrices are $\mathbf{M} = \text{diag} \{ \mathbf{M}_{B_b}, \mathbf{M}_{B_c}, \mathbf{M}_{B_d}, \mathbf{M}_{B_e}, \mathbf{M}_{B_f} \}$, $\mathbf{\Gamma} = \text{diag} \{ \mathbf{\Gamma}_{B_b}, \mathbf{\Gamma}_{B_c}, \mathbf{\Gamma}_{B_d}, \mathbf{\Gamma}_{B_e}, \mathbf{\Gamma}_{B_f} \}$, $\mathbf{K} = \text{diag} \{ \mathbf{K}_{B_b}, \mathbf{K}_{B_c}, \mathbf{K}_{B_d}, \mathbf{K}_{B_e}, \mathbf{K}_{B_f} \}$, $\mathbf{\Omega} = \text{diag} \{ \mathbf{\Omega}_{B_b}, \mathbf{\Omega}_{B_c}, \mathbf{\Omega}_{B_d}, \mathbf{\Omega}_{B_e}, \mathbf{\Omega}_{B_f} \}$, $\mathbf{f}^\top = [\mathbf{f}_{B_b}^\top \ \mathbf{f}_{B_c}^\top \ \mathbf{f}_{B_d}^\top \ \mathbf{f}_{B_e}^\top \ \mathbf{f}_{B_f}^\top]$, and $\mathbf{f}^{non^\top} = [\mathbf{f}_{B_b}^{non^\top} \ \mathbf{f}_{B_c}^{non^\top} \ \mathbf{f}_{B_d}^{non^\top} \ \mathbf{f}_{B_e}^{non^\top} \ \mathbf{f}_{B_f}^{non^\top}]$.

B. Component Assembly Constraints

The base of each boom, B_i , $i \in \{c, d, e, f\}$, is constrained to the perimeter of the spacecraft hub, B_b . This is expressed through the holonomic constraint

$$\mathbf{r}_a^{ia} = \mathbf{r}_a^{ba} + \mathbf{C}_{ab} \mathbf{r}_b^{ib}, \quad (42)$$

where \mathbf{r}_b^{ib} describes the constant position of the boom attachment point on the spacecraft hub relative to its center of mass. Differentiating (42) with respect to time results in

$$\dot{\mathbf{r}}_a^{ia} = \dot{\mathbf{r}}_a^{ba} - \mathbf{C}_{ab} \mathbf{r}_b^{ib \times} \boldsymbol{\omega}_b^{ba},$$

which is used to express the constraint in Pfaffian form as

$$\dot{\mathbf{r}}_a^{ia} - \dot{\mathbf{r}}_a^{ba} + \mathbf{C}_{ab} \mathbf{r}_b^{ib^\times} \boldsymbol{\omega}_b^{ba} = \mathbf{0}. \quad (43)$$

To constrain the booms to be rigidly attached to the spacecraft hub, i.e., the boom base cannot rotate with respect to the hub, the angular velocities of each body relative to an inertial reference frame must be equal ($\boldsymbol{\omega}_i^{ba} = \boldsymbol{\omega}_i^{ia}$). This leads to the following constraint in Pfaffian form,

$$\boldsymbol{\omega}_i^{ia} - \boldsymbol{\omega}_i^{ba} = \mathbf{0}. \quad (44)$$

All of the assembly constraints are then expressed as $\boldsymbol{\Xi} \boldsymbol{\nu} = \mathbf{0}$, where

$$\boldsymbol{\Xi} = \begin{bmatrix} -1 & \mathbf{C}_{ab} \mathbf{r}_b^{cb^\times} & \mathbf{0} & \mathbf{1} & \mathbf{0} & \mathbf{0} & \mathbf{0} & \mathbf{0} & \mathbf{0} & \mathbf{0} & \mathbf{0} & \mathbf{0} & \mathbf{0} & \mathbf{0} \\ -1 & \mathbf{C}_{ab} \mathbf{r}_b^{db^\times} & \mathbf{0} & \mathbf{0} & \mathbf{0} & \mathbf{0} & \mathbf{1} & \mathbf{0} & \mathbf{0} & \mathbf{0} & \mathbf{0} & \mathbf{0} & \mathbf{0} & \mathbf{0} \\ -1 & \mathbf{C}_{ab} \mathbf{r}_b^{eb^\times} & \mathbf{0} & \mathbf{0} & \mathbf{0} & \mathbf{0} & \mathbf{0} & \mathbf{0} & \mathbf{0} & \mathbf{1} & \mathbf{0} & \mathbf{0} & \mathbf{0} & \mathbf{0} \\ -1 & \mathbf{C}_{ab} \mathbf{r}_b^{fb^\times} & \mathbf{0} & \mathbf{0} & \mathbf{0} & \mathbf{0} & \mathbf{0} & \mathbf{0} & \mathbf{0} & \mathbf{0} & \mathbf{0} & \mathbf{0} & \mathbf{1} & \mathbf{0} \\ \mathbf{0} & -\mathbf{C}_{cb} & \mathbf{0} & \mathbf{1} & \mathbf{0} & \mathbf{0} & \mathbf{0} & \mathbf{0} & \mathbf{0} & \mathbf{0} & \mathbf{0} & \mathbf{0} & \mathbf{0} & \mathbf{0} \\ \mathbf{0} & -\mathbf{C}_{db} & \mathbf{0} & \mathbf{0} & \mathbf{0} & \mathbf{0} & \mathbf{1} & \mathbf{0} & \mathbf{0} & \mathbf{0} & \mathbf{0} & \mathbf{0} & \mathbf{0} & \mathbf{0} \\ \mathbf{0} & -\mathbf{C}_{eb} & \mathbf{0} & \mathbf{0} & \mathbf{0} & \mathbf{0} & \mathbf{0} & \mathbf{0} & \mathbf{0} & \mathbf{1} & \mathbf{0} & \mathbf{0} & \mathbf{0} & \mathbf{0} \\ \mathbf{0} & -\mathbf{C}_{fb} & \mathbf{0} & \mathbf{0} & \mathbf{0} & \mathbf{0} & \mathbf{0} & \mathbf{0} & \mathbf{0} & \mathbf{0} & \mathbf{0} & \mathbf{0} & \mathbf{1} & \mathbf{0} \end{bmatrix}. \quad (45)$$

The assembly constraints are added to the aggregate equations of motion in (41) to obtain the system's constrained equations of motion

$$\mathbf{M} \dot{\boldsymbol{\nu}} + \boldsymbol{\Gamma}^\top \mathbf{K} \mathbf{q} + \mathbf{f}^{non} = \boldsymbol{\Gamma}^\top \mathbf{f} + \boldsymbol{\Xi}^\top \boldsymbol{\lambda}, \quad (46)$$

where $\boldsymbol{\lambda}$ contains the Lagrange multipliers that maintain the assembly constraint. Interestingly, the use of the null-space method in the following section will remove the need to compute both the Lagrange multipliers $\boldsymbol{\lambda}$ and the constraint matrix $\boldsymbol{\Xi}$ when numerically solving these equations of motion in simulation.

C. Change of Variables

A reduced set of augmented velocities is chosen as $\hat{\boldsymbol{\nu}}^\top = \left[\dot{\mathbf{r}}_a^{ba^\top} \ \boldsymbol{\omega}_b^{ba^\top} \ \dot{\mathbf{q}}^{\epsilon c^\top} \ \dot{\mathbf{q}}^{\epsilon d^\top} \ \dot{\mathbf{q}}^{\epsilon e^\top} \ \dot{\mathbf{q}}^{\epsilon f^\top} \right]$, which represent a minimal set of generalized velocities needed to represent the constrained motion of the assembled system. The augmented velocities are related to the unconstrained generalized velocities through the Pfaffian form constraints, (43)

and (44), and summarized by the relationship $\boldsymbol{\nu} = \Upsilon \hat{\boldsymbol{\nu}}$. The matrix Υ and its derivative with respect to time are given by

$$\Upsilon^T = \begin{bmatrix} \mathbf{1} & \mathbf{0} & \mathbf{1} & \mathbf{0} & \mathbf{0} & \mathbf{1} & \mathbf{0} & \mathbf{0} & \mathbf{1} & \mathbf{0} & \mathbf{0} & \mathbf{1} & \mathbf{0} & \mathbf{0} \\ \mathbf{0} & \mathbf{1} & \mathbf{r}_b^{cb^\times} \mathbf{C}_{ba} & \mathbf{C}_{bc} & \mathbf{0} & \mathbf{r}_b^{db^\times} \mathbf{C}_{ba} & \mathbf{C}_{bd} & \mathbf{0} & \mathbf{r}_b^{eb^\times} \mathbf{C}_{ba} & \mathbf{C}_{be} & \mathbf{0} & \mathbf{r}_b^{fb^\times} \mathbf{C}_{ba} & \mathbf{C}_{bf} & \mathbf{0} \\ \mathbf{0} & \mathbf{0} & \mathbf{0} & \mathbf{0} & \mathbf{1} & \mathbf{0} & \mathbf{0} & \mathbf{0} & \mathbf{0} & \mathbf{0} & \mathbf{0} & \mathbf{0} & \mathbf{0} & \mathbf{0} \\ \mathbf{0} & \mathbf{0} & \mathbf{0} & \mathbf{0} & \mathbf{0} & \mathbf{0} & \mathbf{0} & \mathbf{1} & \mathbf{0} & \mathbf{0} & \mathbf{0} & \mathbf{0} & \mathbf{0} & \mathbf{0} \\ \mathbf{0} & \mathbf{0} & \mathbf{0} & \mathbf{0} & \mathbf{0} & \mathbf{0} & \mathbf{0} & \mathbf{0} & \mathbf{0} & \mathbf{0} & \mathbf{1} & \mathbf{0} & \mathbf{0} & \mathbf{0} \\ \mathbf{0} & \mathbf{0} & \mathbf{0} & \mathbf{0} & \mathbf{0} & \mathbf{0} & \mathbf{0} & \mathbf{0} & \mathbf{0} & \mathbf{0} & \mathbf{0} & \mathbf{0} & \mathbf{0} & \mathbf{1} \end{bmatrix}, \quad (47)$$

$$\dot{\Upsilon}^T = \begin{bmatrix} \mathbf{0} & \mathbf{0} & \mathbf{0} & \mathbf{0} & \mathbf{0} & \mathbf{0} & \mathbf{0} & \mathbf{0} & \mathbf{0} & \mathbf{0} & \mathbf{0} & \mathbf{0} & \mathbf{0} & \mathbf{0} \\ \mathbf{0} & \mathbf{0} & -\mathbf{r}_b^{cb^\times} \boldsymbol{\omega}_b^{ba^\times} \mathbf{C}_{ba} & \mathbf{0} & \mathbf{0} & -\mathbf{r}_b^{db^\times} \boldsymbol{\omega}_b^{ba^\times} \mathbf{C}_{ba} & \mathbf{0} & \mathbf{0} & -\mathbf{r}_b^{eb^\times} \boldsymbol{\omega}_b^{ba^\times} \mathbf{C}_{ba} & \mathbf{0} & \mathbf{0} & -\mathbf{r}_b^{fb^\times} \boldsymbol{\omega}_b^{ba^\times} \mathbf{C}_{ba} & \mathbf{0} & \mathbf{0} \\ \mathbf{0} & \mathbf{0} & \mathbf{0} & \mathbf{0} & \mathbf{0} & \mathbf{0} & \mathbf{0} & \mathbf{0} & \mathbf{0} & \mathbf{0} & \mathbf{0} & \mathbf{0} & \mathbf{0} & \mathbf{0} \\ \mathbf{0} & \mathbf{0} & \mathbf{0} & \mathbf{0} & \mathbf{0} & \mathbf{0} & \mathbf{0} & \mathbf{0} & \mathbf{0} & \mathbf{0} & \mathbf{0} & \mathbf{0} & \mathbf{0} & \mathbf{0} \\ \mathbf{0} & \mathbf{0} & \mathbf{0} & \mathbf{0} & \mathbf{0} & \mathbf{0} & \mathbf{0} & \mathbf{0} & \mathbf{0} & \mathbf{0} & \mathbf{0} & \mathbf{0} & \mathbf{0} & \mathbf{0} \\ \mathbf{0} & \mathbf{0} & \mathbf{0} & \mathbf{0} & \mathbf{0} & \mathbf{0} & \mathbf{0} & \mathbf{0} & \mathbf{0} & \mathbf{0} & \mathbf{0} & \mathbf{0} & \mathbf{0} & \mathbf{0} \end{bmatrix}. \quad (48)$$

It can be shown that $\Xi \Upsilon = \mathbf{0}$ by substituting $\boldsymbol{\nu} = \Upsilon \hat{\boldsymbol{\nu}}$ into $\Xi \boldsymbol{\nu} = \mathbf{0}$, which is the central property of the null-space method.

D. Constrained Solar Sail Equations of Motion: The Null-Space Method

The null-space method is applied to the equations of motion in (46) by first pre-multiplying on the left by Υ^T , resulting in

$$\Upsilon^T \mathbf{M} \dot{\boldsymbol{\nu}} + \Upsilon^T \boldsymbol{\Gamma}^T \mathbf{K} \mathbf{q} + \Upsilon^T \mathbf{f}^{non} = \Upsilon^T \boldsymbol{\Gamma}^T \mathbf{f} + \Upsilon^T \Xi^T \boldsymbol{\lambda}. \quad (49)$$

With $\Upsilon^T \Xi^T = \mathbf{0}$, the Lagrange multipliers are now removed from (49). The time derivative of the change of coordinate relationship, $\dot{\boldsymbol{\nu}} = \Upsilon \dot{\hat{\boldsymbol{\nu}}} + \dot{\Upsilon} \hat{\boldsymbol{\nu}}$, is then substituted into (49), resulting in

$$\Upsilon^T \mathbf{M} (\Upsilon \dot{\hat{\boldsymbol{\nu}}} + \dot{\Upsilon} \hat{\boldsymbol{\nu}}) + \Upsilon^T \boldsymbol{\Gamma}^T \mathbf{K} \mathbf{q} + \Upsilon^T \mathbf{f}^{non} = \Upsilon^T \boldsymbol{\Gamma}^T \mathbf{f},$$

which can be written in the compact form

$$\bar{\mathbf{M}} \dot{\hat{\boldsymbol{\nu}}} + \bar{\mathbf{K}} \mathbf{q} + \bar{\mathbf{f}}_{non} = \bar{\mathbf{f}}, \quad (50)$$

where $\bar{\mathbf{M}} = \Upsilon^T \mathbf{M} \Upsilon$, $\bar{\mathbf{K}} = \Upsilon^T \boldsymbol{\Gamma}^T \mathbf{K}$, $\bar{\mathbf{f}}_{non} = \Upsilon^T \mathbf{f}^{non} + \Upsilon^T \mathbf{M} \dot{\Upsilon} \hat{\boldsymbol{\nu}}$, and $\bar{\mathbf{f}} = \Upsilon^T \boldsymbol{\Gamma}^T \mathbf{f}$.

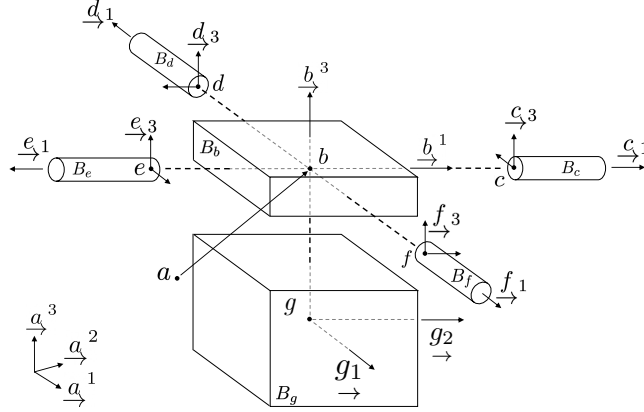


Fig. 18 Exploded view of CABLESSail Assembly #2 consisting of solar sail bus B_b , spacecraft bus B_g , and CABLESSail booms $B_c - B_f$, shortened for clarity, with corresponding body frames and attachment points.

It is worth emphasizing the modularity of equations of motion derived in (50). For example, if a component is to be altered in the assembly or the constrained is to be adjusted, the only changes required are to the constraint matrices, Υ and $\dot{\Upsilon}$, and updating the component sub-matrices within the aggregate matrices \mathbf{M} , \mathbf{K} , $\mathbf{\Gamma}$, etc. with those from the new component. This modularity is reflected in the structure of the numerical simulation code for this system.

E. Second Assembly with Active Mass Translator

A second solar sail component configuration is used in this work and is a modification of the previous model achieved with the null-space method. The previous configuration is modified by including an additional component, the spacecraft bus B_g , and modifying an existing component, the solar sail bus B_b . This is done to model the effect of an active mass translator actuator [11], which has the ability to translate two spacecraft bus components relative to one another. To include the new component the corresponding matrices, generalized coordinates, generalized velocities, and vectors describing the component dynamics from Section IX.B are simply appended to the existing aggregated assembly dynamics \mathbf{M} , \mathbf{K} , $\mathbf{\Gamma}$, $\mathbf{\Omega}$, \mathbf{f} , and \mathbf{f}^{non} . Two additional rows are inserted into $\mathbf{\Xi}$ to enforce the new constraint assembling the new spacecraft bus onto the existing solar sail bus, which are

$$\begin{aligned} \dot{\mathbf{r}}_a^{ga} - \dot{\mathbf{r}}_a^{ba} + \mathbf{C}_{ab} \mathbf{r}_b^{gb \times} \boldsymbol{\omega}_b^{ba} &= \mathbf{0}, \\ \boldsymbol{\omega}_g^{ga} - \boldsymbol{\omega}_g^{ba} &= \mathbf{0}. \end{aligned}$$

The constraint matrix, $\mathbf{\Xi}$, is modified from Assembly #1 with additional zero columns appended to account for the increased length of $\boldsymbol{\nu}$, and the additions of row five and ten that rigidly constrain the spacecraft bus, B_g , to the solar sail bus B_b in translation and rotation, respectively. The actuation position of the AMT is encapsulated within \mathbf{r}_b^{gb} , which describes the position of the spacecraft bus center of mass relative to the solar sail bus center of mass. The form of $\mathbf{\Xi}$ for

this case is given as

$$\mathbb{E} = \begin{bmatrix} -1 & C_{ab}r_b^{cb^\times} & 0 & 1 & 0 & 0 & 0 & 0 & 0 & 0 & 0 & 0 & 0 & 0 & 0 \\ -1 & C_{ab}r_b^{db^\times} & 0 & 0 & 0 & 0 & 1 & 0 & 0 & 0 & 0 & 0 & 0 & 0 & 0 \\ -1 & C_{ab}r_b^{eb^\times} & 0 & 0 & 0 & 0 & 0 & 0 & 0 & 1 & 0 & 0 & 0 & 0 & 0 \\ -1 & C_{ab}r_b^{fb^\times} & 0 & 0 & 0 & 0 & 0 & 0 & 0 & 0 & 0 & 1 & 0 & 0 & 0 \\ -1 & C_{ab}r_b^{gb^\times} & 0 & 0 & 0 & 0 & 0 & 0 & 0 & 0 & 0 & 1 & 0 & 0 & 0 \\ 0 & -C_{cb} & 0 & 1 & 0 & 0 & 0 & 0 & 0 & 0 & 0 & 0 & 0 & 0 & 0 \\ 0 & -C_{db} & 0 & 0 & 0 & 0 & 1 & 0 & 0 & 0 & 0 & 0 & 0 & 0 & 0 \\ 0 & -C_{eb} & 0 & 0 & 0 & 0 & 0 & 0 & 0 & 1 & 0 & 0 & 0 & 0 & 0 \\ 0 & -C_{fb} & 0 & 0 & 0 & 0 & 0 & 0 & 0 & 0 & 0 & 1 & 0 & 0 & 0 \\ 0 & -C_{gb} & 0 & 0 & 0 & 0 & 0 & 0 & 0 & 0 & 0 & 1 & 0 & 0 & 0 \end{bmatrix}.$$

The change of variables is modified from Assembly #2 by appending two additional rows to the matrices Υ and $\dot{\Upsilon}$ defined in (47) and (48). Specifically, the additional rows appended to the end of Υ are given by

$$\begin{bmatrix} 1 & -C_{ab}r_b^{gb^\times} & 0 & 0 & 0 & 0 \\ 0 & C_{gb} & 0 & 0 & 0 & 0 \end{bmatrix},$$

while the rows appended to $\dot{\Upsilon}$ are

$$\begin{bmatrix} 0 & -C_{ab}\omega_b^{ba^\times}r_b^{gb^\times} & 0 & 0 & 0 & 0 \\ 0 & 0 & 0 & 0 & 0 & 0 \end{bmatrix}.$$

Funding Sources

This work was supported by an Early Career Faculty grant from NASA's Space Technology Research Grants Program under award No. 80NSSC23K0075.

References

- [1] Gong, S., and Macdonald, M., "Review on Solar Sail Technology," *Astrodynamics*, Vol. 3, No. 2, 2019, pp. 93–125. <https://doi.org/10.1007/s42064-019-0038-x>.
- [2] Thomas, D., Baysinger, M., Sutherlin, S., Bean, Q., Clements, K., Kobayashi, K., Garcia, J., Fabisinski, L., and Capizzo, P.,

- “Solar Polar Imager Concept,” *ASCEND*, Virtual Event, 2020. <https://doi.org/10.2514/6.2020-4060>, AIAA 2020-4060.
- [3] Kobayashi, K., Johnson, L., Thomas, H., McIntosh, S., McKenzie, D., Newmark, J., Heaton, A., Carr, J., Baysingere, M., Bean, Q., et al., “The High Inclination Solar Mission,” *arXiv preprint arXiv:2006.03111*, 2020. <https://doi.org/10.48550/arXiv.2006.03111>.
- [4] Spencer, D. A., Betts, B., Bellardo, J. M., Diaz, A., Plante, B., and Mansell, J. R., “The LightSail 2 Solar Sailing Technology Demonstration,” *Advances in Space Research*, Vol. 67, No. 9, 2021, pp. 2878–2889. <https://doi.org/10.1016/j.asr.2020.06.029>.
- [5] Wilkie, W. K., Fernandez, J. M., Stohlman, O. R., Schneider, N. R., Dean, G. D., Kang, J. H., Warren, J. E., Cook, S. M., Brown, P. L., Denkins, T. C., Horner, S. D., Tapio, E. D., Straubel, M., Richter, M., and Heiligers, J., “Overview of the NASA Advanced Composite Solar Sail System (ACS3) Technology Demonstration Project,” *AIAA Scitech Forum*, Virtual Event, 2021. <https://doi.org/10.2514/6.2021-1260>, AIAA 2021-1260.
- [6] Berthet, M., Schalkwyk, J., Çelik, O., Sengupta, D., Fujino, K., Hein, A. M., Tenorio, L., Cardoso dos Santos, J., Worden, S. P., Mauskopf, P. D., Miyazaki, Y., Funaki, I., Tsuji, S., Fil, P., and Suzuki, K., “Space Sails for Achieving Major Space Exploration Goals: Historical Review and Future Outlook,” *Progress in Aerospace Sciences*, Vol. 150, 2024, p. 101047. <https://doi.org/10.1016/j.paerosci.2024.101047>.
- [7] Pimienta-Penalver, A., Tsai, L.-W., Juang, J.-N., and Crassidis, J. L., “Heliogyro Solar Sail Structural Dynamics and Stability,” *Journal of Guidance, Control, and Dynamics*, Vol. 42, No. 8, 2019, pp. 1645–1657. <https://doi.org/10.2514/1.G003758>.
- [8] Brownell, M., Sinclair, A. J., and Singla, P., “A Time-Varying Subspace Method for Shape Estimation of a Flexible Spacecraft Membrane,” *AIAA SciTech Forum*, National Harbor, MD, 2023. <https://doi.org/10.2514/6.2023-2068>, AIAA 2023-2068.
- [9] Boni, L., Bassetto, M., Niccolai, L., Mengali, G., Quarta, A. A., Circi, C., Pellegrini, R. C., and Cavallini, E., “Structural Response of Helianthus Solar Sail During Attitude Maneuvers,” *Aerospace Science and Technology*, Vol. 133, 2023. <https://doi.org/10.1016/j.ast.2023.108152>.
- [10] Gauvain, B. M., and Tyler, D. A., “A Solar Sail Shape Modeling Approach for Attitude Control Design and Analysis,” *6th International Symposium on Space Sailing*, New York, NY, 2023.
- [11] Inness, J., Tyler, D., Diedrich, B., Ramazani, S., and Orphee, J., “Momentum Management Strategies for Solar Cruiser and Beyond,” *6th International Symposium on Space Sailing*, New York, NY, 2023.
- [12] Wie, B., and Murphy, D., “Solar-Sail Attitude Control Design for a Flight Validation Mission,” *Journal of Spacecraft and Rockets*, Vol. 44, No. 4, 2007, pp. 809–821. <https://doi.org/10.2514/1.22996>.
- [13] Bolle, A., and Circi, C., “Solar Sail Attitude Control Through In-Plane Moving Masses,” *Proceedings of the Institution of Mechanical Engineers, Part G: Journal of Aerospace Engineering*, Vol. 222, No. 1, 2008, pp. 81–94. <https://doi.org/10.1243/09544100JAERO22>.

- [14] Lappas, V., Mengali, G., Quarta, A. A., Gil-Fernandez, J., Schmidt, T., and Wie, B., “Practical Systems Design for an Earth-Magnetotail-Monitoring Solar Sail Mission,” *Journal of Spacecraft and Rockets*, Vol. 46, No. 2, 2009, pp. 381–393. <https://doi.org/10.2514/1.32040>.
- [15] Romagnoli, D., and Oehlschlägel, T., “High Performance Two Degrees of Freedom Attitude Control for Solar Sails,” *Advances in Space Research*, Vol. 48, No. 11, 2011, pp. 1869–1879. <https://doi.org/10.1016/j.asr.2011.04.027>.
- [16] Adeli, S. N., Lappas, V. J., and Wie, B., “A Scalable Bus-Based Attitude Control System for Solar Sails,” *Advances in Space Research*, Vol. 48, No. 11, 2011, pp. 1836–1847. <https://doi.org/10.1016/j.asr.2011.08.024>.
- [17] Huang, H., and Zhou, J., “Solar Sailing CubeSat Attitude Control Method with Satellite as Moving Mass,” *Acta Astronautica*, Vol. 159, 2019, pp. 331–341. <https://doi.org/10.1016/j.actaastro.2019.03.077>.
- [18] Firuzi, S., and Gong, S., “Attitude Control of a Flexible Solar Sail in Low Earth Orbit,” *Journal of Guidance, Control, and Dynamics*, Vol. 41, No. 8, 2018, pp. 1715–1730. <https://doi.org/10.2514/1.G003178>.
- [19] Wie, B., “Solar Sail Attitude Control and Dynamics, Part 2,” *Journal of Guidance, Control, and Dynamics*, Vol. 27, No. 4, 2004, pp. 536–544. <https://doi.org/10.2514/1.11133>.
- [20] Sperber, E., Fu, B., and Eke, F. O., “Large Angle Reorientation of a Solar Sail Using Gimballed Mass Control,” *The Journal of the Astronautical Sciences*, Vol. 63, No. 2, 2016, pp. 103–123. <https://doi.org/10.1007/s40295-016-0085-1>.
- [21] Funase, R., Mimasu, Y., Chishiki, Y., Shirasawa, Y., Tsuda, Y., Saiki, T., and Kawaguchi, J., “Modeling and On-Orbit Performance Evaluation of Propellant-Free Attitude Control System for Spinning Solar Sail via Optical Parameter Switching,” *AAS/AIAA Astrodynamics Specialist Conference*, Girdwood, AK, 2012, pp. 1737–1754.
- [22] Borggräfe, A., Heiligers, J., Ceriotti, M., and McInnes, C., “Optical Control of Solar Sails Using Distributed Reflectivity,” *Spacecraft Structures Conference*, National Harbor, MD, 2014. <https://doi.org/10.2514/6.2014-0833>, AIAA 2014-0833.
- [23] Ullery, D. C., Soleymani, S., Heaton, A., Orphee, J., Johnson, L., Sood, R., Kung, P., and Kim, S. M., “Strong Solar Radiation Forces From Anomalously Reflecting Metasurfaces for Solar Sail Attitude Control,” *Scientific Reports*, Vol. 8, No. 1, 2018, pp. 1–10. <https://doi.org/10.1038/s41598-018-28133-2>.
- [24] Davoyan, A. R., Munday, J. N., Tabiryan, N., Swartzlander, G. A., and Johnson, L., “Photonic Materials for Interstellar Solar Sailing,” *Optica*, Vol. 8, No. 5, 2021, pp. 722–734. <https://doi.org/10.1364/OPTICA.417007>.
- [25] Qi, X., Fan, C., and He, G., “A Novel Unloading Strategy for Solar Sails Using Reflectivity Control Device,” *Journal of Physics. Conference Series*, Vol. 2764, No. 1, 2024, p. 012066. <https://doi.org/10.1088/1742-6596/2764/1/012066>.
- [26] Choi, M., and Damaren, C. J., “Structural dynamics and attitude control of a solar sail using tip vanes,” *Journal of Spacecraft and Rockets*, Vol. 52, No. 6, 2015, pp. 1665–1679. <https://doi.org/10.2514/1.A33179>.
- [27] Eldad, O., Lightsey, E. G., and Claudel, C., “Minimum-Time Attitude Control of Deformable Solar Sails with Model Uncertainty,” *Journal of Spacecraft and Rockets*, Vol. 54, No. 4, 2017, pp. 863–870. <https://doi.org/10.2514/1.A33713>.

- [28] Hassanpour, S., and Damaren, C. J., “Collocated Attitude and Vibrations Control for Square Solar Sails with Tip Vanes,” *Acta Astronautica*, Vol. 166, 2020, pp. 482–492. <https://doi.org/10.1016/j.actaastro.2019.07.038>.
- [29] Eldad, O., and Lightsey, E. G., “Propellantless Attitude Control of a Nonplanar Solar Sail,” *Journal of Guidance, Control, and Dynamics*, Vol. 38, No. 8, 2015, pp. 1531–1534. <https://doi.org/10.2514/1.G001135>.
- [30] Choi, M., and Damaren, C. J., “Control Allocation of Solar Sail Tip Vanes with Two Degrees of Freedom,” *Journal of Guidance, Control, and Dynamics*, Vol. 39, No. 8, 2016, pp. 1857–1865. <https://doi.org/10.2514/1.G001703>.
- [31] Chujo, T., “Propellant-Free Attitude Control of Solar Sails with Variable-Shape Mechanisms,” *Acta Astronautica*, Vol. 193, 2022, pp. 182–196. <https://doi.org/10.1016/j.actaastro.2021.12.044>.
- [32] Guerrant, D., and Lawrence, D., “Tactics for Heliogyro Solar Sail Attitude Control via Blade Pitching,” *Journal of Guidance, Control, and Dynamics*, Vol. 38, No. 9, 2015, pp. 1785–1799. <https://doi.org/10.2514/1.G000861>.
- [33] Fu, B., and Eke, F. O., “Attitude Control Methodology for Large Solar Sails,” *Journal of Guidance, Control, and Dynamics*, Vol. 38, No. 4, 2015, pp. 662–670. <https://doi.org/10.2514/1.G000048>.
- [34] Fu, B., Sperber, E., and Eke, F., “Solar Sail Technology—A State of the Art Review,” *Progress in Aerospace Sciences*, Vol. 86, 2016, pp. 1–19. <https://doi.org/10.1016/j.paerosci.2016.07.001>.
- [35] Caverly, R. J., Bunker, K. R., Raab, N., Nguyen, V. L., Saner, G., Chen, Z., Douvier, T., Lyman, R. J., Sorby, O., Sorge, B., Teshale, E., and Toriseva, B., “Solar Sail Attitude Control Using Shape Modulation: The Cable-Actuated Bio-inspired Lightweight Elastic Solar Sail (CABLESSail) Concept,” *6th International Symposium on Space Sailing*, New York, NY, 2023.
- [36] Zhang, F., Shengping, G., Haoran, G., and Baoyin, H., “Solar Sail Attitude Control Using Shape Variation of Booms,” *Chinese Journal of Aeronautics*, Vol. 35, No. 10, 2021, pp. 326–336. <https://doi.org/10.1016/j.cja.2021.10.036>.
- [37] Zhang, F., Gong, S., and Baoyin, H., “Three-Axes Attitude Control of Solar Sail Based on Shape Variation of Booms,” *Aerospace*, Vol. 8, No. 8, 2021, p. 198. <https://doi.org/10.3390/aerospace8080198>.
- [38] Papadopoulos, E., Aghili, F., Ma, O., and Lampariello, R., “Robotic Manipulation and Capture in Space: A Survey,” *Frontiers in Robotics and AI*, Vol. 8, 2021, p. 686723. <https://doi.org/10.3389/frobt.2021.686723>.
- [39] Hughes, P. C., *Spacecraft Attitude Dynamics*, Dover Publications, Mineola, NY, 2004.
- [40] de Ruiter, A. H. J., Damaren, C. J., and Forbes, J. R., *Spacecraft Dynamics and Control: An Introduction*, John Wiley and Sons, Chichester, UK, 2013.
- [41] Bunker, K. R., and Caverly, R., “Modular Dynamic Modeling and Simulation of a Cable-Actuated Flexible Solar Sail,” *AIAA SciTech Forum*, Orlando, FL, 2024. <https://doi.org/10.2514/6.2024-2436>, AIAA 2024-2436.
- [42] Heaton, A. F., and Artusio-Glimpse, A., “An Update to the NASA Reference Solar Sail Thrust Model,” *AIAA SPACE Conference and Exposition*, Pasadena, CA, 2015. <https://doi.org/10.2514/6.2015-4506>, AIAA 2015-4506.

- [43] Satou, Y., Okuizumi, N., Sakamoto, H., Furuya, H., Ono, G., Shirasawa, Y., and Mori, O., “Nonflatness of Solar Sail Membrane Predicted by Nonlinear Finite Element Analyses,” *AIAA SciTech Forum*, National Harbor, MD, 2014. <https://doi.org/10.2514/6.2014-0832>, AIAA 2014-0832.
- [44] Okuizumi, N., Satou, Y., Mori, O., Sakamoto, H., and Furuya, H., “Analytical Investigation of Global Deployed Shape of a Spinning Solar Sail Membrane,” *AIAA Journal*, Vol. 59, No. 3, 2021, pp. 1075–1086. <https://doi.org/10.2514/1.J059717>.
- [45] Nguyen, L., Medina, K., McConnel, Z., and Lake, M. S., “Solar Cruiser TRAC Boom Development,” *AIAA SciTech Forum*, National Harbor, MD, 2023. <https://doi.org/10.2514/6.2023-1507>, AIAA 2023-1507.
- [46] Johnson, L., and Curran, F., “Solar Cruiser Technology Maturation Plans,” Tech. Rep. 20205003681, NASA Marshall Space Flight Center, 2020.
- [47] Heaton, A., Ramazani, S., and Tyler, D., “Reflectivity Control Device (RCD) Roll Momentum Management for Solar Cruiser and Beyond,” *6th International Symposium on Solar Sailing*, New York, NY, 2023.
- [48] de Ruiter, A. H. J., and Forbes, J. R., “General Identities for Parameterizations of $SO(3)$ With Applications,” *Journal of Applied Mechanics*, Vol. 81, No. 071007, 2014. <https://doi.org/10.1115/1.4027144>.
- [49] Rao, S. S., *Vibration of Continuous Systems*, Wiley, Hoboken, NJ, 2019.
- [50] Damaren, C., and Sharf, I., “Simulation of Flexible-Link Manipulators with Inertial and Geometric Nonlinearities,” *Journal of Dynamic Systems, Measurement, and Control*, Vol. 111, No. 1, 1995, pp. 74–87. <https://doi.org/10.1115/1.2798525>.